ROYAL SOCIETY
OF CHEMISTRY

FEATURE ARTICLE

Check for updates

Interface phenomena and emerging functionalities in ferroelectric oxide based heterostructures

Yifei Hao, [iD] Tianlin Li [iD] and Xia Hong [iD] *

Capitalizing on the nonvolatile, nanoscale controllable polarization, ferroelectric perovskite oxides can be integrated with various functional materials for designing emergent phenomena enabled by charge, lattice, and polar symmetry mediated interfacial coupling, as well as for constructing novel energy-efficient electronics and nanophotonics with programmable functionalities. When prepared in thin film or membrane forms, the ferroelectric instability of these materials is highly susceptible to the interfacial electrostatic and mechanical boundary conditions, resulting in tunable polarization fields and Curie temperatures and domain formation. This review focuses on two types of ferroelectric oxide-based heterostructures: the epitaxial perovskite oxide heterostructures and the ferroelectric oxides interfaced with two-dimensional van der Waals materials. The topics covered include the basic synthesis methods for ferroelectric oxide thin films, membranes, and heterostructures, characterization of their properties, and various emergent phenomena hosted by the heterostructures, including the polarization-controlled metal–insulator transition and magnetic anisotropy, negative capacitance effect, domain-imposed one-dimensional graphene superlattices, programmable second harmonic generation, and interface-enhanced polar alignment and piezoelectric response, as well as their applications in nonvolatile memory, logic, and reconfigurable optical devices. Possible future research directions are also outlined, encompassing the synthesis *via* remote epitaxy and oxide moiré engineering, incorporation of binary ferroelectric oxides, realization of topological properties, and functional design of oxygen octahedral rotation.

1. Introduction

Ferroelectrics possess nonvolatile, spontaneous polarization that is switchable *via* an external electric field (Fig. 1). When they are prepared in thin film forms, the ferroelectric free energy is highly susceptible to the electrostatic and mechanical boundary conditions, which can be utilized to engineer the polar properties and control domain formation.[1–3] The heterostructures interfacing ferroelectrics with other nanoscale functional materials thus present a versatile platform for designing emergent ferroic orders and exploring novel control mechanisms that are not viable in single-phase materials. Leveraging the voltage-controlled nature and nanoscale programmable polarization, ferroelectric thin films have been widely adopted to construct energy-efficient electronic devices, including ferroelectric field effect transistors (FeFETs),[4] ferroelectric tunnel junctions (FTJs),[5] memristors,[6] and negative capacitance (NC) transistors,[7] which are promising building blocks for developing low-power memory and logic applications as

well as neuromorphic computing. Their polar properties have also been exploited in intriguing mechanical[8] and optical[9] applications.

Compared with the widely studied ferroelectric polymer and van der Waals (vdW) materials, ferroelectric perovskite oxides are known for their large polarization, high dielectric constant, high ferroelectric Curie temperature (T_C), low coercive field (E_c), and unit-cell-scale sharp domain walls (DWs).[1] For ferroelectric perovskite thin films and membranes, the interfacial layers play a critical role in determining the material parameters and even affecting the ferroelectric instability. Capitalizing on the interfacial coupling mediated by charge, strain, and polar symmetry, ferroelectric oxides have been utilized to modulate the electronic, magnetic, and optical properties of the neighboring materials.[4,10–14] Various emergent phenomena have been reported in ferroelectric oxide-based heterostructures, including polarization-controlled quantum phase transitions,[15,16] polar vortices,[17,18] negative capacitance mode,[19,20] enhanced polar alignment,[21,22] periodic domain structure imposed superlattices,[23] and unconventional nonlinear optical filtering effects.[24,25] The ability to synthesize single crystalline ferroelectric oxide membranes[26–29] and stack them with controlled twist angles[29] lifts the lattice constraints for

Department of Physics and Astronomy & Nebraska Center for Materials and Nanoscience, University of Nebraska-Lincoln, Lincoln, NE, 68588-0299, USA. E-mail: xia.hong@unl.edu
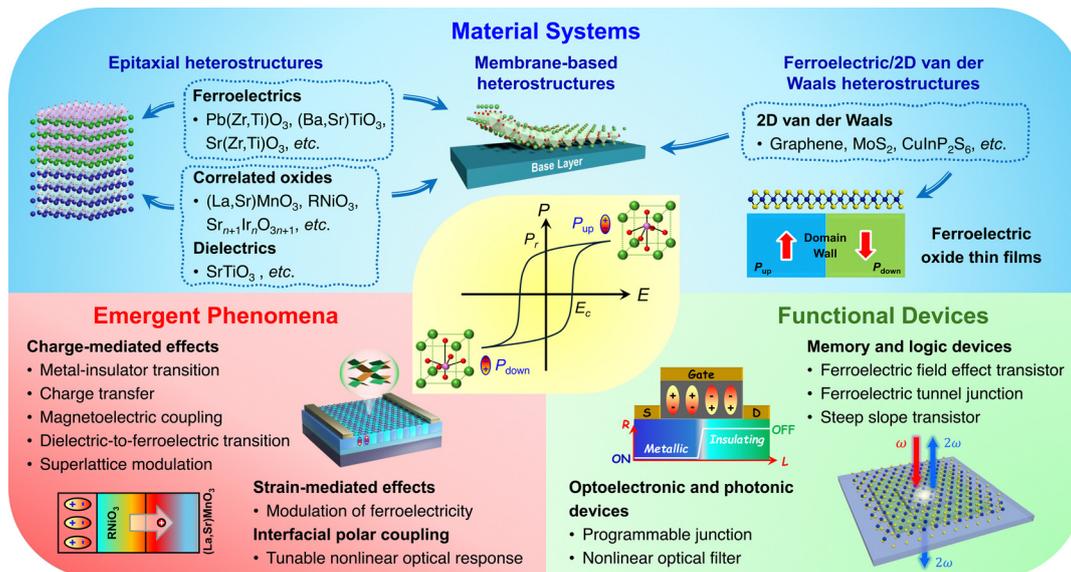
Fig. 1 Overview of research on ferroelectric perovskite oxide-based heterostructures, including material systems, emergent phenomena, and potential device applications. P_{up}/P_{down}: polarization up/down.

building multifunctional heterointerfaces and opens up the opportunity to develop oxide-based twistronics. The advancements in the growth of crystalline ferroelectric perovskites on conventional semiconductors such as Si[30,31] and Ge[32] herald the potential to integrate these emergent functionalities with the mainstream semiconductor industry.

In this feature article, we focus on two types of ferroelectric oxide-based heterostructures, the epitaxial complex oxide heterostructures and the ferroelectric thin films and membranes interfaced with two-dimensional (2D) van der Waals materials, discussing the basic synthesis methods and property characterization and surveying a range of interface phenomena and emerging functionalities. In Section 2, we discuss the synthesis and characterization of different types of heterostructures. Section 3 summarizes the effects of the interfacial layer on the ferroelectric properties of epitaxial oxide thin films and free-standing membranes. Section 4 focuses on the epitaxial ferroelectric oxide heterostructures, discussing the polarization control of the electronic and magnetic properties of correlated oxides, the ferroelectric-to-dielectric transition, domain formation, and transient NC effect in ferroelectric/dielectric oxide heterostructures, as well as related device concepts such as Mott FeFETs and all-oxide FTJs. Section 5 centers on the ferroelectric/ 2D van der Waals heterostructures, discussing the ferroelectric field effect, domain induced superlattice modulation, tuning of second harmonic generation, and enhanced polar alignment and piezoelectric response in 2D ferroelectrics, as well as highlighting the potential applications in electron lensing, NC FETs, and programmable nonlinear optical filters. Section 6 summarizes the research progress and provides an outlook on possible future directions, such as novel synthesis *via* remote epitaxy and oxide moiré engineering, incorporation of doped ferroelectric hafnia and zirconia, realization of topological properties, and functional design of oxygen octahedral rotation.

2. Materials synthesis and characterization

2.1 Epitaxial ferroelectric oxide heterostructures

The rapid development of advanced physical vapor deposition (PVD) techniques enables scalable growth of high quality epitaxial thin films of ferroelectric oxides. For perovskite transition metal oxides, their structural and chemical similarities allow the combination of ferroelectric oxides with various functional oxides, ranging from dielectrics to Mott insulators, magnets, and superconductors, into high-quality epitaxial heterostructures.[11] The atomic registration between interfacial constituent layers can not only eliminate dangling bonds, minimizing defect formation, but also enable novel lattice design *via* controlling lattice strain[33] and oxygen octahedral rotation.[34] In addition to the charge mediated coupling mechanism, strain-induced lattice distortion and migration of defects such as oxygen vacancies can also have a profound impact on the physical properties.

For epitaxial complex oxide thin film deposition, widely used PVD techniques[35] include molecular-beam epitaxy (MBE), pulsed laser deposition (PLD), and off-axis radio-frequency (RF) magnetron sputtering. In this paper, we center on the discussions of epitaxial ferroelectric thin films and heterostructures prepared *via* the off-axis RF magnetron sputtering approach. Examples include the ferroelectric/correlated oxide and ferroelectric/dielectric perovskite heterostructures. Compared with the MBE and PLD methods, magnetron sputtering has the advantages of low growth temperature, compatibility with industrial scale deposition, and low cost. The sputtering technique has recently been utilized to prepare polar nitride perovskites,[36] which broadens the class of materials viable for exploring polarization-based phenomena and device applications.[37] One limitation of the sputtering growth is that the strong magnetic field precludes the implementation of the reflection high-energy electron diffraction
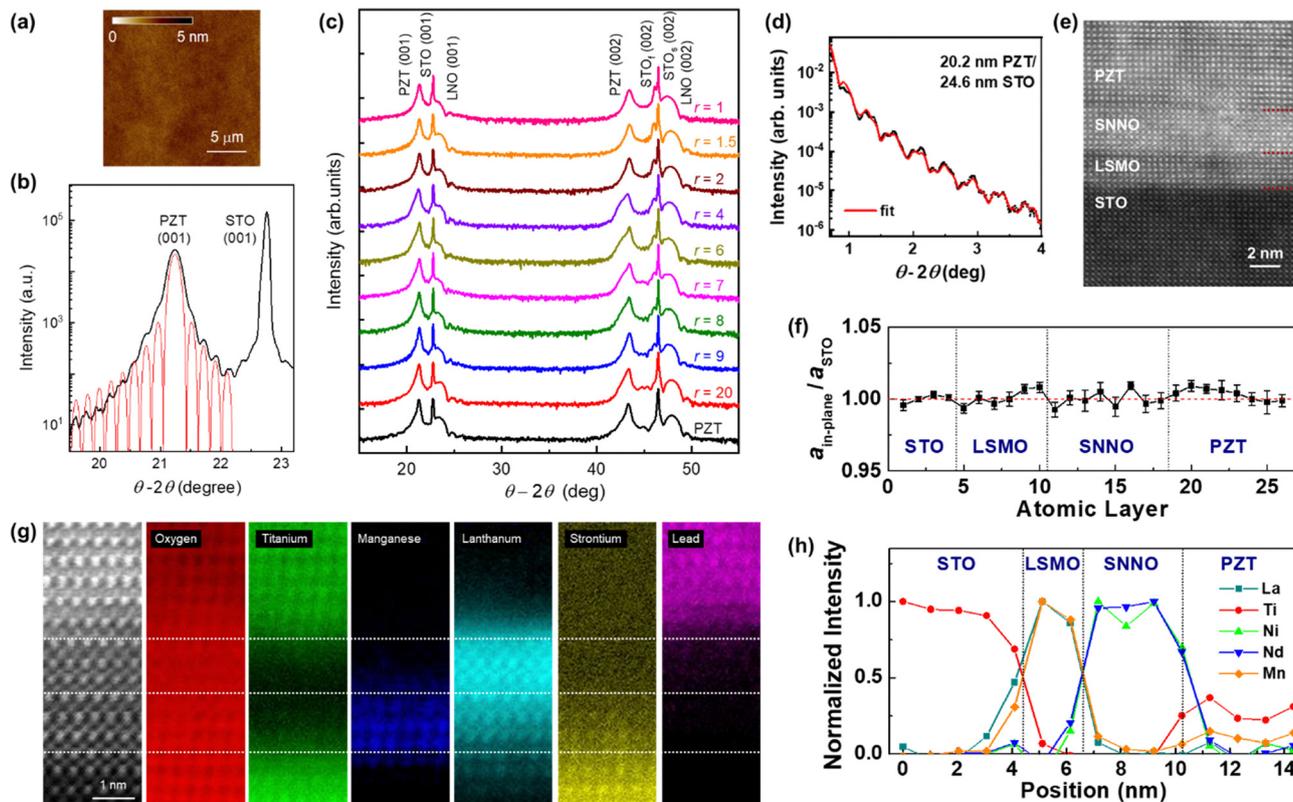
Fig. 2 Characterization of epitaxial PZT heterostructures. (a) AFM topography image and (b) XRD $\theta-2\theta$ scan taken on 50 nm PZT/10 nm LSMO on (001) STO, with a fit to the Laue oscillations around the (001) peak of PZT (red line). Reproduced from ref. 23 with permission from American Physical Society, copyright 2024. (c) XRD $\theta-2\theta$ scans taken on PZT/STO heterostructures with a total thickness of about 100 nm deposited on LNO buffered STO substrates with different PZT and STO layer thickness ratios ($r = t_{PZT}/t_{STO}$). (d) XRR performed on a PZT/STO heterostructure. Reproduced from ref. 39 with permission from American Physical Society, copyright 2021. (e) HRSTEM and (f) in-plane lattice constants of different layers normalized to that of STO substrate for a PZT/3 nm SNNO/2 nm LSMO heterostructure. Reproduced from ref. 40 with permission from Wiley-VCH GmbH, copyright 2017. (g) HRSTEM (left panel) and EELS element mapping performed on a PZT/3 uc LNO/3 uc LSMO heterostructure. Reproduced from ref. 41 with permission from Springer Nature, copyright 2023. (h) EELS line scans for five elements taken on the sample shown in (e) and (f). Reproduced from ref. 40 with permission from Wiley-VCH GmbH, copyright 2017.

(RHEED) technique for *in situ* characterization of sample crystallinity and growth mode. Efforts have been made to incorporate RHEED into sputtering *via* special sputtering chamber design, such as adopting antisymmetric sputter sources.[38]

The PVD techniques can yield single crystalline thin films and heterostructures with high crystallinity, atomically flat surfaces, and unit-cell-level precise control of film thickness. Fig. 2 shows the surface, structural, and chemical properties of ferroelectric $PbZr_{0.2}Ti_{0.8}O_3$ (PZT) interfaced with dielectric oxide $SrTiO_3$ (STO) and strongly correlated oxides such as $RNiO_3$ (RNO with R = Sm, Nd, or La) and $La_{0.67}Sr_{0.33}MnO_3$ (LSMO). These samples possess smooth surface morphology, as revealed by atomic force microscopy (AFM). Fig. 2(a) shows the AFM image taken on a 50 nm PZT/10 nm LSMO heterostructure deposited on a (001) STO substrate with a root-mean-square (RMS) roughness of 4–5 Å.[23] X-ray diffraction (XRD) measurements of these heterostructures reveal the (001) growth of all layers (Fig. 2(b) and (c)).[23,39] Fig. 2(c) shows the XRD spectra taken on a series of PZT/STO heterostructures with about 100 nm total thickness deposited on 10 nm $LaNiO_3$ (LNO) buffered STO.[39] Regardless of the layer thickness, the *c*-axis of

PZT is about 4.17 ± 0.1 Å, consistent with the strained value on STO, showing that epitaxial strain can sustain in 100 nm thickness films.

Even though real-time monitoring of the growth rate is not available for these sputtered samples, the highly smooth sample surfaces/interfaces allow post-growth thickness characterization *via* either the Laue oscillations around the main Bragg peaks (Fig. 2(b) and (c))[23,39] or X-ray reflectivity (XRR) (Fig. 2(d))[39] measurements, which can be used to calibrate the deposition rate. Transmission electron microscopy (TEM) studies confirm that precise thickness control has been achieved. Fig. 2(e) shows the high-resolution scanning TEM (HRSTEM) image of a PZT/ 3 nm $Sm_{0.5}Nd_{0.5}NiO_3$ (SNNO)/2 nm LSMO heterostructure,[40] which reveals high crystallinity and atomically sharp interfaces. The in-plane lattice constant for each atomic layer has been deduced from the TEM data, confirming that the entire heterostructure is fully strained to the STO substrate (Fig. 2(f)).[40] Fig. 2(g) shows the electron energy loss spectroscopy (EELS) elemental mapping of a PZT/1.2 nm LNO/1.2 nm LSMO heterostructure,[41] showing that the interfaces are also chemically sharp. The line profiles of the EELS data (Fig. 2(h)) indicate

that the diffusion of interfacial atoms is typically within one-to-two unit cell (uc) scale.[40,41]

2.2 Free-standing ferroelectric oxide membranes

Recent developments in the synthesis of single crystalline complex oxide membranes[42,43] further broaden the material design portfolio for ferroelectric oxide-based heterostructures, opening up new avenues for exploring novel interface phenomena and achieving tailored functionalities.[25,28,29,44–47] In particular, it is possible to construct heterostructures with the same constituents either in the epitaxial heterointerface form or *via* direct contact of membranes. Comparing the physical properties of these two types of systems helps differentiate the effects of electrostatic and mechanical boundary conditions on the ferroelectric instability in perovskite thin films. Building twisted ferroelectric oxide heterostructures further broadens the parameter space for engineering novel polar states,[29] which are not bound by the intrinsic crystal symmetry. Epitaxial ferroelectric oxide thin films can be suspended from the substrate *via* depositing on a water soluble layer such as $Sr_3Al_2O_6$ (SAO) (Fig. 3(a)) followed by water etching[28,42] or through selected chemical etching of a buffer layer such as $(La,Sr)MnO_3$.[29,44]
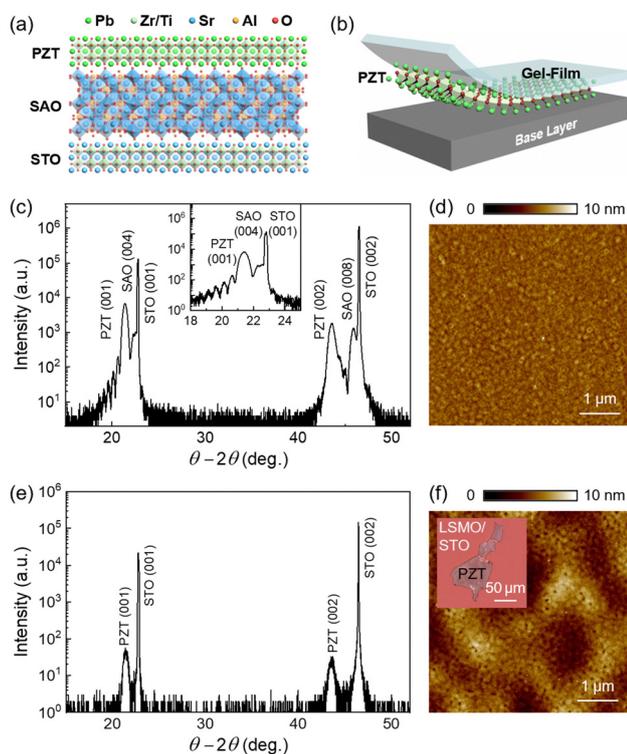

Fig. 3 Preparation and characterization of PZT membranes. (a) Schematic of a PZT/SAO heterostructure on STO. (b) Schematic of dry transfer of a PZT membrane on a designated base layer. (c) XRD $\theta-2\theta$ scan and (d) AFM topography image taken on 50 nm PZT/20 nm SAO on (001) STO. (e) XRD $\theta-2\theta$ scan of the same sample after water etching of the SAO layer. (f) AFM topography image a PZT flake transferred on a LSMO/STO base layer. Inset: Optical image of the flake. Reproduced from ref. 28 with permission from American Chemical Society, copyright 2023.

Table 1 Effect of the buffer/base layer on the properties of epitaxial PZT films, PZT membranes, and PZT/LSMO membranes. The T_C values are extracted from the thermal-quenching experiments performed on 50 nm PZT thin films and membranes. The data for epitaxial thin films are from ref. 48. The data for membranes are from ref. 28

Sample	Buffer/ base layer	Surface roughness (film thickness) (nm)	E_c (MV cm^{-1})		T_C (°C)
			P_{up}	P_{down}	
Epitaxial PZT	LSMO	0.4 (50)	−0.5	+1.1	775 ± 25
	LaNiO$_3$	0.2 (50)	−0.56	+0.38	738 ± 12
	SrIrO$_3$	0.3 (50)	−0.1	+0.36	775 ± 25
PZT membrane	Au	2.0 (20)	−3.0	+1.7	763 ± 12
	LSMO	1.0 (20)	−1.70	+1.09	725 ± 25
	MoS$_2$	0.3 (20)	−1.60	+0.75	588 ± 12
PZT/LSMO membrane	Au	0.8 (20)	−0.18	+0.74	
	LSMO	0.5 (20)	−0.26	+0.28	
	MoS$_2$	0.4 (20)	−0.6	+1.01	

The freestanding membranes can then be transferred on any designated base layer using Gel-Film[28] or PMMA[47] with precision control of position and orientation (Fig. 3(b)).

Fig. 3(c)–(f) compares the crystallinity and surface roughness of a 50 nm PZT film deposited on 20 nm SAO buffered STO before and after water-etching. The epitaxial heterostructure possesses single crystalline (001) PZT and SAO layers with no impurity phases (Fig. 3(c)) and smooth surface morphology with an RMS roughness of about 5 Å (Fig. 3(d)). After water-etching, the SAO peaks disappear, while the suspended PZT layer retains the crystallinity (Fig. 3(e)) and shows the same *c*-axis lattice constant of 4.15 Å, suggesting that the PZT membrane remains fully strained even after suspension from the substrate. Fig. 3(f) shows the AFM image of a 20 nm PZT membrane transferred on a LSMO/STO base layer. The flake exhibits clear ripples, with the RMS roughness (∼1 nm) significantly higher than the roughness of the base layer (∼4 Å) (Table 1). In contrast, the 20 nm PZT/10 nm LSMO membrane on LSMO/STO exhibits a surface roughness similar to the base layer, suggesting that atomic bonding with the LSMO layer effectively reduces rippling.

2.3 Ferroelectric oxide/2D van der Waals heterostructures

Integrating ferroelectric oxides with 2D van der Waals materials can enable functional design of the electronic, mechanical, and optical responses *via* ferroelectric field effect doping, strain modulation, and nanoscale domain control.[4,14] The van der Waals layers can be interfaced with single-crystalline[49–53] and polycrystalline ferroelectric thin films,[54–56] ferroelectric single crystals,[57,58] and ferroelectric oxide membranes.[25,28,44–46] Compared with the epitaxial thin films, large-scale, low-cost synthesis of polycrystalline ferroelectric oxide films can be achieved by chemical vapor deposition (CVD) methods such as the metal–organic CVD[59] approach and the sol–gel method.[60] While these techniques are desirable for industrial processing, the polycrystalline samples exhibit compromised polarization and high density structural defects such as grain boundaries.

The 2D van der Waals layers can be prepared on the ferroelectric oxide substrates *via* direct mechanical exfoliation,[49,50] dry transfer,[23,25,28] or direct CVD growth.[58] The direct mechanical exfoliation method exploits adhesive tape to peel off 2D atomic layers from high-quality single crystals and lay the resulting flakes directly on the ferroelectric substrates.[61] It preserves to the maximum extent the intrinsic properties of the 2D materials, while the limitations include low yield, lack of thickness control, presence of tape residue, and difficulty in identifying atomically thin flakes on ferroelectric oxides due to low optical contrast.[49,56] To increase the yield and flake size for mechanical exfoliation, substrate treatments with oxygen plasma[62] or metal-film-coating[63] have been developed to enhance the interaction between the substrate and van der Waals materials. By pre-patterning interaction-enhanced regions, it is possible to have 2D vdW flakes directly exfoliated onto specific locations on the substrate, resulting in complex architectures unattainable with conventional exfoliation and dry-transfer methods. While these interaction-enhancement approaches have been successfully applied to a wide range of 2D materials to achieve up to millimeter-scale exfoliation,[62–65] they may alter the surface chemistry of the ferroelectric oxides or produce undesired interfacial layers, which compromise the device functionality.

In the dry-transfer method, viscoelastic polymer films such as polydimethylsiloxane (PDMS),[66] polypropylene carbonate (PPC),[67,68] and polycarbonate (PC)[69] serve as transfer stamps to pick up and drop down pre-prepared 2D vdW flakes, which facilitates precise positioning and stacking-order control for heterostructure fabrication. The pick-up and drop-down processes are controlled by adjusting the vitrification of polymer films at different temperatures, while the transfer process is guided by an actuated x–y–z–θ-stage, enabling sub-micron-scale precision in alignment and placement of 2D flakes on the oxide substrate, as well as control over interlayer twist angles. The dry nature of the transfer process ensures that the interface remains uncontaminated, as it avoids solvent exposure until the final cleaning step for removing polymer residues. Additionally, encapsulation with air-stable top layers such as hexagonal boron nitride (h-BN) protects the vdW surface from direct exposure to the ambient conditions, which is critical for preserving the intrinsic properties of 2D materials that are sensitive to moisture.[70]

Bottom-up synthesis techniques, such as CVD, physical vapor transport, and MBE, have also been developed for fabricating 2D vdW flakes, thin films, and heterostructures.[71–73] For example, monolayer MoS_2 has been directly grown on a periodically poled $LiNbO_3$ substrate, which shows a preferred growth on the P_{up} domains.[58] It is conceivable that scalable synthesis of 2D vdW thin films directly on the ferroelectric substrate can facilitate the development of industrial applications of ferroelectric oxide/2D vdW heterostructures. A major material challenge is that most of these techniques involve high temperature synthesis in high/ultrahigh vacuum, which can exceed the structural phase transition temperatures of some widely used ferroelectric oxides (*e.g.*, $BaTiO_3$)[74] and introduce oxygen vacancies,[75] therefore compromising the device performance.

3. Interface effects on ferroelectric properties

3.1 Epitaxial ferroelectric thin films

Various ferroelectric properties of ferroelectric oxide thin films, including polarization, E_c, T_C, and domain wall roughness and creep behaviors, have been investigated using electrical measurements and scanning probe microscopy. The results reveal the profound effects of electrostatic and mechanical boundary conditions on ferroelectricity and domain formation. Fig. 4(a) shows the characterization of polarization *vs.* electric field (P–E) loops taken on an Au/100 nm PZT/10 nm LaNiO$_3$ capacitor, where the polarization is calculated by integrating the charging and discharging current through the circuit upon polarization switching.[39] The deduced remanent polarization is about 78 μC cm^{-2}, consistent with those obtained from Hall effect measurements of epitaxial FeFETs.[41,76] The coercive field increases with increasing frequency (f) of the bias voltage (V_{bias}) wave, with E_c exhibiting a power-law dependence on f (Fig. 4(b)),[39] which can be well described by the domain nucleation and growth dominated polarization switching process.[77]

Conductive AFM and piezoresponse force microscopy (PFM) have been used to assess polarization switching, write/image domain structures, and quantify the piezoelectric coefficients. Fig. 4(c) and (d) shows the PFM images of concentric square domains written on a PZT/LSMO heterostructure *via* conductive AFM, which shows that the as-grown sample is uniformly polarized in the P_{up} state.[48] Fig. 4(e) and (f) shows the PFM switching hysteresis taken on this sample, which reveals a smaller coercive voltage for the P_{up} state than that for the P_{down}
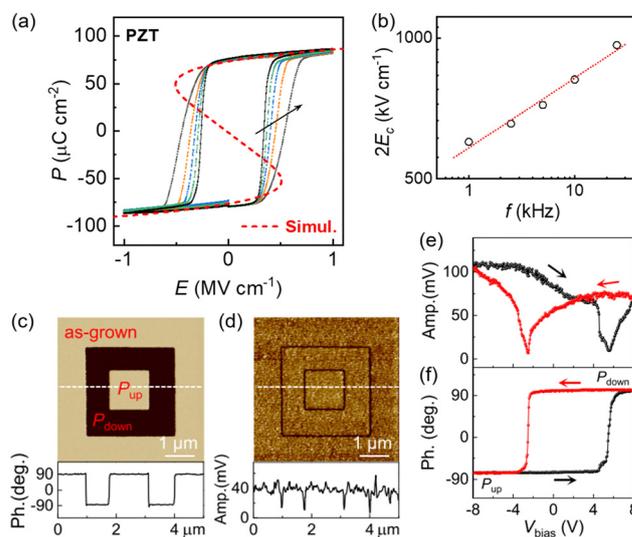

Fig. 4 Ferroelectric properties of PZT thin films. (a) P–E loops at different V_{bias} frequencies, and (b) $2E_c$ *vs.* f for an Au/100 nm PZT/10 nm LaNiO$_3$ capacitor on STO. Reproduced from ref. 39 with permission from American Physical Society, copyright 2021. (c)–(f) PFM studies of a 50 nm PZT/10 nm LSMO heterostructure on STO. (c) PFM phase and (d) amplitude images of concentric square domains. (e) PFM amplitude and (f) phase switching hysteresis. Reproduced from ref. 48 with permission from American Physical Society, copyright 2021.

state, consistent with the as-grown polarization, confirming that the P_{up} state is energetically favorable. The polarization asymmetry has been widely observed in epitaxial PZT thin films and depends sensitively on the choice of correlated oxide electrodes (Table 1).[48] Quantitatively analyzing the PFM amplitude response *vs.* V_{bias} below the coercive field can yield the piezoelectric coefficient.[21,22]

PFM studies have also been utilized to assess T_C, polarization switching dynamics, and the static configuration of DWs in epitaxial ferroelectric thin films. Due to the compressive strain, epitaxial PZT thin films deposited on (001) SrTiO$_3$ substrates normally exhibit significantly higher T_C compared with the bulk value ($T_C \sim 450$ °C[78]). Fig. 5(a) shows the PFM images of stripe domains written on a PZT/LSMO heterostructure on SrTiO$_3$, where the sample has been heated at progressively higher temperatures and quenched rapidly to room temperature.[48] The domain structure remains stable after thermal-quench (TQ) cycles at temperatures of up to 600 °C. Bubble domains

start to emerge at 650 °C, while the originally straight DWs become barely recognizable at 750 °C. Similar results have been observed in PZT films with LaNiO$_3$ and SrIrO$_3$ (SIO) bottom electrodes, showing that T_C for PZT strained on SrTiO$_3$ is above 700 °C (Table 1).[48] The high thermal stability makes epitaxial PZT thin films viable for high temperature applications.

For industrial applications, there has been extensive research interest in integrating ferroelectric perovskites with conventional semiconductors.[79,80] Besides canonical ferroelectrics such as PZT[30] and BaTiO$_3$,[31] perovskite oxides that are non-ferroelectric in bulk such as STO[81] and Sr(Zr,Ti)O$_3$ (SZTO)[32] can develop a ferroelectric relaxor phase in strained thin films. Fig. 5(b) shows the PFM amplitude response of P_{up} and P_{down} domains patterned on a 15 nm SZTO film deposited on Ge. The amplitude signal relaxes initially with a power-law time dependence $t^{-\alpha}$ and then stabilizes at about 10 hours, remaining stable after 48 hours of domain writing. The exponents are $\alpha = 0.22$ for the P_{up} state and $\alpha = 0.23$ for the P_{down} state, which are consistent with strained STO that exhibits relaxor behavior.[82]

Despite the similar T_C, the PZT films deposited on different correlated oxide electrodes exhibit distinct thermal evolution of DW roughness due to the collective contributions of interfacial screening condition and defect migration. For ferroelectrics, the DW roughness carries important information about the dimensionality, disorder type, and nature of interaction of the system,[83,84] which can be quantitatively assessed by calculating the correlation function of the relative transverse displacement (u) of two points along the DW separated by a distance L (Fig. 5(c) inset): $B(L) = \overline{\left\langle [u(x+L) - u(x)]^2 \right\rangle}$, which averages over position and disorder distribution. Treating DW as an elastic manifold in a disordered medium, $B(L)$ exhibits a power-law dependence on L, $B(L) \propto L^{2\zeta}$, where ζ is the roughness exponent. Previous PFM studies have shown that the DW roughening of epitaxial PZT thin films exhibits 2D random bond (RB) disorder dominated behavior with long range dipole interaction ($\zeta_{2D,RB} = 0.31$) at room temperature[85] and evolves to a one-dimensional (1D) thermal roughening ($\zeta_{1D,TF} = 0.5$) dominated behavior at high temperatures.[48,86] DW roughening due to 1D RB behavior ($\zeta_{1D,RB} = 2/3$) has been theoretically predicted[87] but has been scarcely observed experimentally in epitaxial thin films, which can be affected by the artificial domain writing process, the ambient screening condition, and the relative energy and length scales of DW elasticity, thermal fluctuation, and disorder pinning.[87–90]

In ref. 48, Wang *et al.* investigated the effect of the correlated oxide electrode on the thermal evolution of DW roughness in PZT. Fig. 5(d) shows ζ *vs.* TQ temperature for 50 nm PZT films deposited on SrTiO$_3$ buffered by 10 nm LSMO, LaNiO$_3$, and SrIrO$_3$ electrodes. For all samples, the ζ values exhibit 2D RB behavior at room temperature and approach 1D thermal roughening behavior close to T_C. The DW growth can be treated as the creep motion of particles in a disorder energy landscape, where thermal fluctuation promotes the de-trapping of DW from the local pinning potential (Fig. 5(e)). The transition temperatures where ζ starts to deviate from $\zeta_{2D,RB}$ (T_{cr}) and
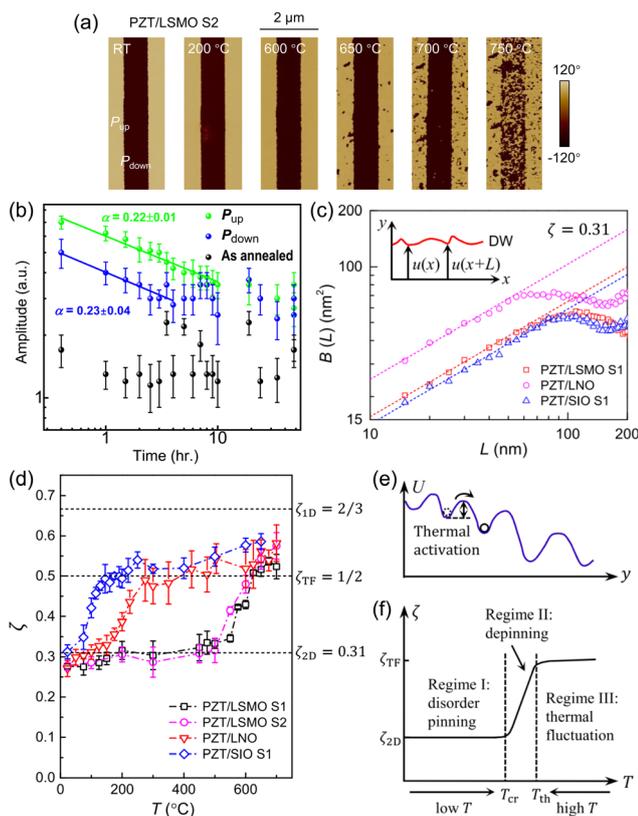

Fig. 5 PFM characterization of ferroelectric perovskite oxide thin films. (a) PFM phase images of a domain structure in PZT/LSMO on STO at selected TQ temperatures. Reproduced from ref. 48 with permission from American Physical Society, copyright 2021. (b) PFM amplitude response *vs.* time with fits to $t^{-\alpha}$ taken on a 15 nm SZTO film on Ge. The power exponents are labelled. Adapted from ref. 32 with permission from American Chemical Society, copyright 2017. (c) DW roughness correlation relation $B(L)$ *vs.* L for 50 nm PZT films on 10 nm correlate oxide electrodes. Inset: Schematic of a rough DW. (d) ζ *vs.* TQ temperature. (e) Schematic of thermally activated DW motion in a disorder energy landscape tilted by an external field. (f) Schematic ζ–T diagram. Reproduced from ref. 48 with permission from American Physical Society, copyright 2021.

where ζ approaches $\zeta_{1D,TF}$ (T_{th}) correspond to the lower and higher bound of the pinning energy, respectively (Fig. 5(f)).[48] PZT on LSMO exhibits the highest transition temperatures, while PZT on $SrIrO_3$ exhibits the lowest, which can be attributed to the effects of lattice distortion and the oxygen migration induced interfacial biasing field. In the former mechanism, LSMO possesses the largest oxygen octahedral rotation and $SrIrO_3$ is the closest to the cubic structure that is closely matched with PZT.[91–94] For the latter, the oxygen migration energy is the lowest in LSMO and the highest in $SrIrO_3$, which can result in different trapping energies at the PZT interface.[95–98] For devices using ferroelectric domains as the information storage unit, the DW roughness determines how closely two bits can be placed without interfering with each other, its temperature response determines the thermal stability of the bit, and E_c determines the writing voltage. Understanding the effect of the electrode material is thus critical for designing the storage density, operation temperature, and energy consumption of PZT-based memory applications, as further illustrated in the ferroelectric membranes.

3.2 Ferroelectric membranes

In ref. 28, Wu *et al.* examined the E_c (Fig. 6(a) and (b)) and T_C (Fig. 6(c)) of PZT and PZT/LSMO membranes prepared on three types of base layers with distinct screening capacities and surface roughness, the metallic Au, correlated LSMO, and semiconducting MoS_2 (Table 1). For single-layer 20 nm PZT membranes, E_c is the highest on Au and lowest on MoS_2 (E_c(Au) > E_c(LSMO) > E_c(MoS_2)), which has been attributed to the change in membrane surface roughness and base layer screening capacity. The rippling of membranes induces a flexoelectric effect, which suppresses DW motion and enhances E_c.[26] The base layer with low conductivity can lead to a high depolarization field, suppress the ferroelectric double well energy, and thus reduce E_c. For comparison, the membranes of PZT/LSMO heterostructures possess a

smoother surface morphology compared with the PZT membranes and exhibit significantly smaller E_c on the same type of base layer (Fig. 6(b)). Among these samples, the PZT/LSMO membrane on the LSMO base layer exhibits symmetric switching with the smallest average E_c value (Table 1). This is significantly lower than those of PZT membranes on LSMO and epitaxial PZT/LSMO heterostructures, despite the same screening electrode (LSMO), clearly illustrating the critical role of the mechanical boundary conditions (*e.g.*, interface roughness and epitaxy) in determining the polarization switching dynamics.

Fig. 6(c) shows the PFM images of thermally quenched stripe domains written on a 50 nm PZT membrane on Au. For all three types of base layers, the PZT membranes exhibit enhanced T_C well exceeding the bulk value (Table 1), consistent with the XRD result showing that the membranes can retain the strain state (Fig. 3(c) and (e)). The membrane on MoS_2 possesses the lowest T_C (> 575 °C), suggesting that the atomically smooth van der Waals type interface may facilitate strain relaxation. At room temperature, PZT membranes thicker than 10 nm and PZT/LSMO membranes on all types of base layers exhibit 2D RB disorder dominated behavior with ζ close to $\zeta_{2D,RB}$ (Fig. 7(a)). For the 10 nm PZT membrane on Au, ζ approaches $\zeta_{1D,TF}$. As the Au film possesses the highest surface roughness, the rippled membrane is partially decoupled from the substrate, which may release it from interface-induced DW pinning, allowing 1D thermal fluctuation dominated DW roughening. Similar to that of epitaxial PZT films (Fig. 5(d)), ζ increases with increasing TQ temperatures (Fig. 7(b)). For the 50 nm PZT membrane on MoS_2, ζ increases to $\zeta_{1D,TF}$ at $T_{th} \sim 500$ °C. Despite the much higher T_C, PZT membranes on LSMO and Au base layers exhibit a much lower T_{cr}. The ζ values quickly exceed $\zeta_{1D,TF}$ and approach $\zeta_{1D,RB}$, suggesting a DW creep
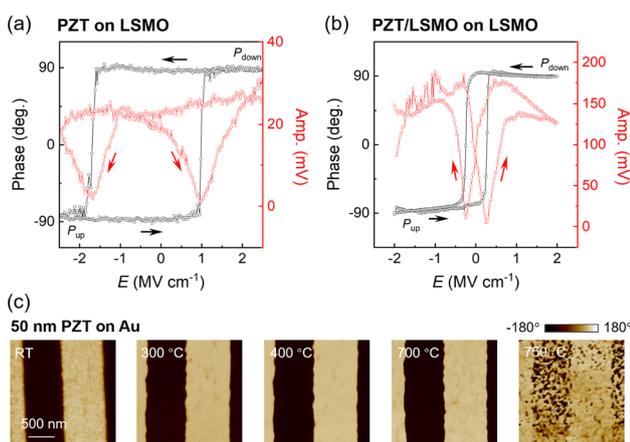

Fig. 6 PFM characterization of PZT and PZT/LSMO membranes. (a) and (b) PFM phase and amplitude switching hysteresis taken on a 20 nm PZT membrane (a) and a 20 nm PZT/10 nm LSMO membrane (b) on LSMO base layers. (c) PFM phase images of stripe domains on a 50 nm PZT membrane on Au at selected TQ temperatures showing a T_C > 750 °C. Reproduced from ref. 28 with permission from American Chemical Society, copyright 2023.
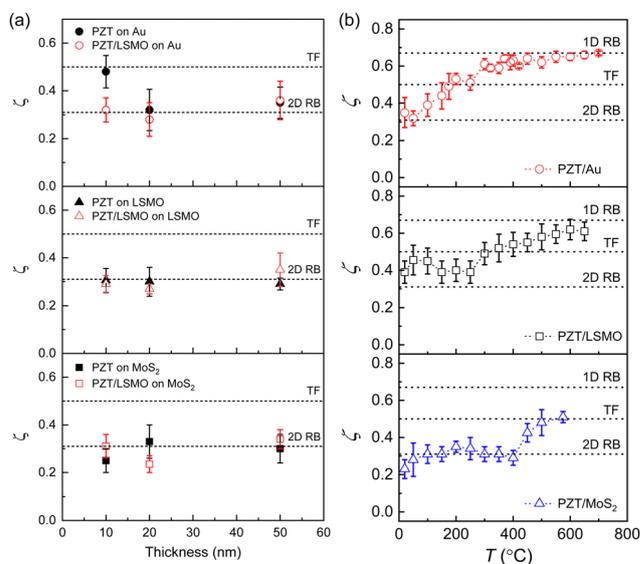

Fig. 7 DW roughness in PZT membranes. (a) ζ *vs.* PZT thickness at room temperature for PZT and PZT/LSMO membranes on different base layers. (b) ζ *vs.* TQ temperature for 50 nm PZT membranes on different base layers. Reproduced from ref. 28 with permission from American Chemical Society, copyright 2023.

behavior within the quasi-equilibrium-nucleation model.[87] Such 1D RB disorder dominated DW roughness has not been observed in epitaxial PZT films at large length scales,[88] and the equilibrium configuration may be established in the PZT membranes due to partial decoupling from the LSMO and Au base layers. The distinct E_c and thermal evolution of DW roughness for PZT membranes on different base layers illustrate the convoluted effects of rippling induced flexoelectric effects, local strain distribution, interface induced DW pinning, and mobility of charged disorders in determining DW motion.[28]

4. Epitaxial ferroelectric oxide heterostructures

4.1 Ferroelectric/correlated oxide heterostructures

4.1.1 Ferroelectric polarization control of correlated transport. For a correlated oxide channel, a ferroelectric gate can be utilized to impose electric field effect doping, strain modulation, and interfacial orbital design, which are powerful means to tune the competing energy scales without introducing

Fig. 8 Ferroelectric field effect in PZT-gated correlated channels. (a) Device schematic. (b) $R_\square(T)$ of 4 nm $La_{0.8}Sr_{0.2}MnO_3$ on STO for both polarization states. Adapted from ref. 100 with permission from American Physical Society, copyright 2019. (c) $R_\square(T)$ of 2.5 nm and 4 nm SNNO channels on $LaAlO_3$ for both polarization states. Inset: Resistance on/off ratio vs. temperature. Reproduced from ref. 40 with permission from Wiley-VCH GmbH, copyright 2017. (d) $R_\square(T)$ of a 1.5 nm $LaNiO_3$ channel for both polarization states. (e) Resistance on/off ratio of single-layer $RNiO_3$ channels vs. channel thickness at 300 K. Adapted from ref. 41 with permission from Springer Nature, copyright 2023.

additional defect states.[10,11] It also facilitates the development of novel high density, energy-efficient electronic devices, such as Mott FeFETs[39,40] and all-oxide ferroelectric or multiferroic tunnel junctions.[99] The ferroelectric field effect has been exploited to tune the transport properties of a wide variety of correlated oxides. As shown in Fig. 8(a), switching the polarization of a ferroelectric top-gate can either accumulate or deplete charge carriers at the interfacial layer of the correlated oxide channel, which can induce conductivity modulation or even a metal–insulator transition. Fig. 8(b) shows the temperature dependence of sheet resistance $R_\square$ of a 4 nm $La_{0.8}Sr_{0.2}MnO_3$ channel in both polarization states of the PZT gate. Switching the polarization leads to a nonvolatile shift of 25 K of resistance peak temperature,[100] which is related to the modulation of T_C.[15,101]

The optimal channel thickness for the ferroelectric field effect modulation is determined by the interfacial charge screening effect and electronic finite size effect. As switching the polarization field yields a fixed 2D density modulation, $2P = \Delta n_{2D}$, the fractional change of 3D carrier density in the channel scales inversely with the channel thickness. On the other hand, the thickness scaling cannot be sustained when the film becomes electrically dead, a phenomenon widely observed in epitaxial correlated oxide thin films,[16,41,102,103] as strongly localized charges cannot provide proper screening for the polarization field, which leads to poor retention behavior for the off state.[40,76] Fig. 8(c) shows the $R_\square(T)$ of 4 nm and 2.5 nm $Sm_{0.5}Nd_{0.5}NiO_3$ devices for both polarization states of PZT.[40] At 300 K, the resistance switching ratio $\Delta R/R_{on}$ for the 2.5 nm channel is about one order of magnitude higher than that of the 4 nm SNNO. For 4 nm SNNO, $\Delta R/R_{on}$ exhibits a peak at 160 K, which is in the vicinity of the metal–insulator transition temperature. Such transition is absent in the 2.5 nm channel as it is below the electrical dead layer thickness. Close to the electrical dead layer thickness, it is possible to induce a carrier density-driven metal–insulator transition via the ferroelectric field effect.[16] Fig. 8(d) shows the $R_\square(T)$ of a 1.5 nm, or 4 uc, $LaNiO_3$ channel for both polarization states of the PZT gate. Bulk $LaNiO_3$ is a correlated metal, while the P_{down} state of PZT depletes holes from $LaNiO_3$ and induces an insulating state.[41]

Fig. 8(e) summarizes the channel thickness (t_{RNO}) dependence of $\Delta R/R_{on}$ at 300 K in single-layer $RNiO_3$ channels.[41] $NdNiO_3$ (NNO), SNNO, and $SmNiO_3$ (SNO) are charge-transfer type Mott insulators with progressively lower charge itinerancy due to a higher degree of lattice distortion.[91,104] Despite the distinct metallicity, the $LaNiO_3$, $NdNiO_3$, and SNNO channels exhibit highly consistent exponential growth of $\Delta R/R_{on}$ with decreasing t_{RNO} until the electrical dead layer thickness is reached, clearly pointing to the interfacial charge screening scenario. $LaNiO_3$ possesses the smallest electrical dead layer thickness of about 2 uc, and the 2 uc $LaNiO_3$ channel exhibits the largest resistance modulation. The corresponding resistance on–off ratio is about 17, which is the highest room temperature value reported for oxide FeFETs with single-layer Mott channels.[41] The maximum $\Delta R/R_{on}$ are smaller in NNO (2.5 uc channel) and SNNO (6.5 uc channel), which can be attributed to the larger electrical dead layer thicknesses.
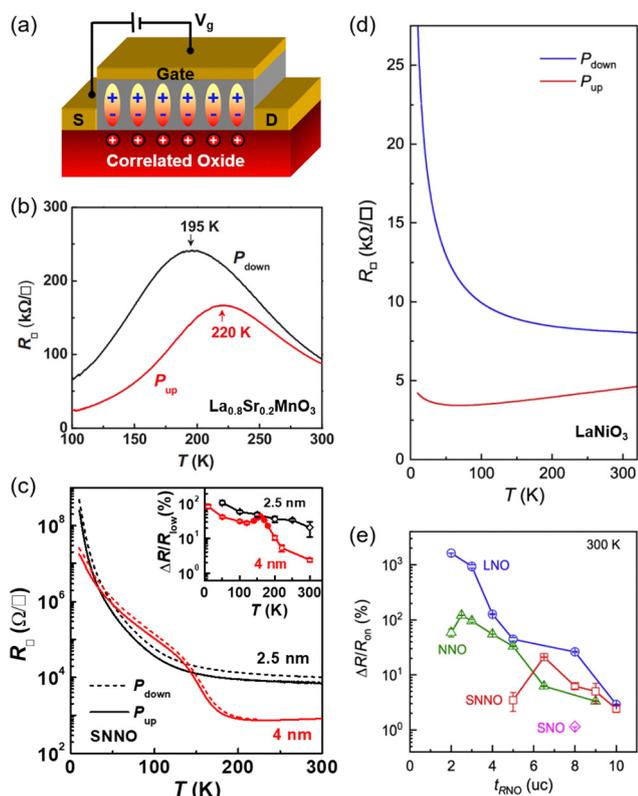
The field effect is negligibly small in SNO, which is insulating in bulk at 300 K. The channel thickness scaling behavior reflects the convoluted effects of carrier density modulation and charge itinerancy in determining the ferroelectric field effect, while strain-induced lattice distortion, interfacial lattice/orbital effects, and size-induced dimensionality crossover can all affect the metallicity of the system.[105–107] Understanding their impacts is critical for developing device applications such as the Mott FeFETs and all-oxide FTJs discussed below.

4.1.2 Interfacial charge engineering of high-performance Mott FeFETs. Mott FETs with metallic carrier density have been proposed as a promising device solution to transcend the size scaling limit of Si-based CMOS technology.[108,109] However, the sheet carrier density in nanoscale correlated oxide thin films can reach 10^{14}–10^{16} cm^{-2} in the metallic state, well exceeding the doping capacity of conventional dielectrics such as SiO_2 and HfO_2.[4] Ferroelectric perovskites such as PZT provide a viable gate choice for Mott transistors as switching the polarization field corresponds to $\Delta n_{2D} \sim 1 \times 10^{15}$ cm^{-2} (Fig. 3(b)).[41,76] Moreover, the nonvolatile, voltage-controlled nature of FeFETs is desirable for energy-efficient device operation. Capitalizing on the high quality epitaxial heterointerface, all-perovskite FeFETs based on a correlated oxide channel has been extensively investigated over the last three decades for developing low-power electronic applications such as nonvolatile memories.[110] The key challenges for practical implementation of this device concept is the competing material requirements for enhancing the resistance switching ratio and optimizing the device retention. As shown in Fig. 8(e), the channel thickness scaling of $\Delta R/R_{on}$ is limited by the electrical dead layer thickness, beyond which strong depolarization field causes severe polarization back-switching and fast relaxation of the resistance states,[40,76] compromising the field effect modulation. To date, the highest room temperature on–off ratio in a single-layer correlated channel is about 17, observed in 2 uc LaNiO$_3$.[41]

One solution to reduce the net carrier density in the Mott channel without causing severe depolarization in the ferroelectric gate is to exploit the charge transfer effect between two correlated oxides to create a tailored density profile in the Mott channel. It has been shown that inserting an LSMO buffer layer with intrinsically low carrier density in RNO$_3$-based Mott FeFETs can significantly enhance the resistance on–off ratio by orders of magnitude.[40,41] The interfacial charge transfer between RNiO$_3$ and LSMO corresponds to the valence change of $Ni^{3+} + Mn^{3+} \rightarrow Ni^{2+} + Mn^{4+}$. Fig. 9 shows the high-angle-annular-dark-field (HAADF) STEM image and EELS elemental mapping of Mn L spectra taken on a PZT/3 uc LNO/3 uc LSMO heterostructure. The atomic layer-by-atomic layer mapping of the Mn valence state (Fig. 9(c) and (d)) reveals about 0.7 eV shift of the Mn L$_3$ peak position, corresponding to 0.06 e^-/Mn transfer from Mn to Ni ions. XAS and XPS studies also point to a charge transfer of 0.08–0.09 e^-/Mn at the Sm$_{0.5}$Nd$_{0.5}$NiO$_3$/LSMO interface,[40] and the experimental results are well corroborated by density functional theory calculations.[40,41] The charge transfer effectively reduces the carrier density in RNiO$_3$ within 1–2 uc at the LNO/LSMO interface (Fig. 9(d)), while the high carrier density at the PZT/LNO interface is sustained.
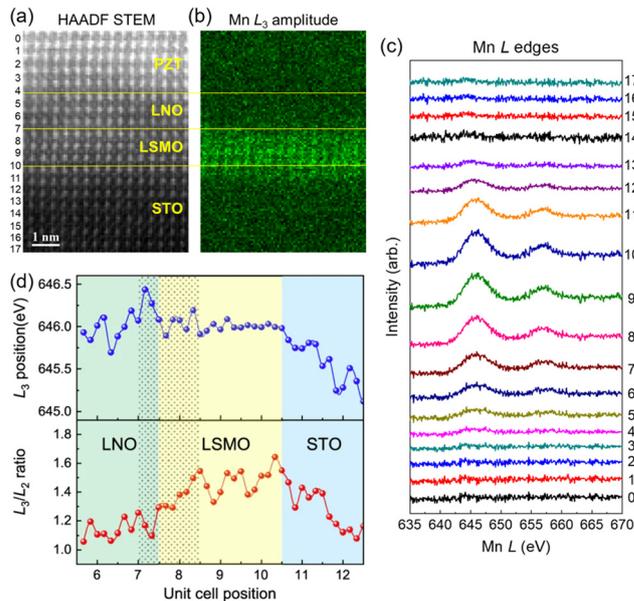

Fig. 9 TEM characterization of a PZT/3 uc LNO/3 uc LSMO heterostructure. (a) Cross-sectional HRSTEM image. (b) EELS elemental mapping of Mn. (c) Layer-by-layer EELS spectra of the Mn L edge. The unit cell positions are labeled in (a). (d) Mn L$_3$ peak position (top) and L$_3$/L$_2$ intensity ratio (bottom) as a function of unit cell position. Adapted from ref. 41 with permission from Springer Nature, copyright 2023.

Fig. 10 compares the resistance switching of FeFETs with single-layer and bilayer correlated channels with similar total channel thickness. For a 4 uc LaNiO$_3$ channel (Fig. 10(a)) and a 3 uc LNO/1 uc LSMO channel (Fig. 10(b)), the resistance on/off ratio ($r_{off/on}$) in the bilayer channel is more than 40 times higher. Increasing the LNO single-layer channel thickness to 5 uc leads to smaller resistance modulation (Fig. 10(c)), as the bottom layer can be treated as a shunting resistor. On the other hand, the ferroelectric field effect in the LNO/LSMO bilayer cannot be modeled as parallel conduction of two independent channels. Increasing the LSMO layer thickness by 1 uc significantly enhances, rather than attenuates, the resistance modulation (Fig. 10(d)), clearly illustrating the effect of interface synergy between LNO and LSMO. Fig. 10(e) summarizes the $\Delta R/R_{on}$ of RNO/LSMO bilayer channels with different layer thickness combinations, which increases exponentially with decreasing total channel thickness (t_{tot}). The universal channel thickness scaling behavior for the Mott FeFETs with both single-layer and bilayer channels clearly testify to the interfacial screening nature of the ferroelectric field effect. For the same t_{tot}, $r_{off/on}$ in the bilayer channel can be over two orders of magnitude higher than that of single-layer RNiO$_3$, pointing to a highly effective approach for designing the ferroelectric field effect. Fig. 10(f) compares the maximum room temperature $\Delta R/R_{on}$ vs. channel thickness ($t_{channel}$) obtained on epitaxial complex oxide FeFETs with different correlated oxide channels, including cuprate,[111,112] cobaltate,[113] manganite,[16,114] ruthenate,[115] single-layer nickelate,[40,41] and bilayer RNiO$_3$/LSMO[40,41] channels. The PZT/2.5 uc LNO/2 uc LSMO device exhibits a record high room temperature $r_{off/on}$ of 385.4, well exceeding the state-of-the-art results for MRAM.[116]
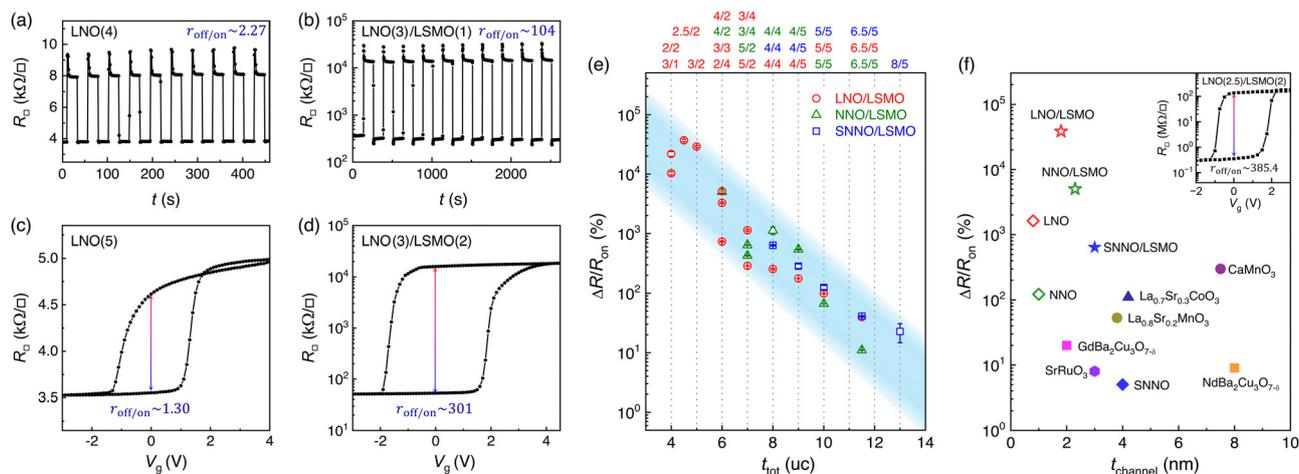
Fig. 10 Room temperature resistance modulation in ferroelectric-gated LNO and LNO/LSMO channels. (a) and (b) $R_\square$ switching upon pulsed gate voltage V_g taken on 4 uc LNO (a) and 4 uc LNO/1 uc LSMO (b) channels. (c) and (d) $R_\square$ vs. V_g switching hysteresis taken on 5 uc LNO (c) and 3 uc LNO/2 uc LSMO (d) channels. (e) $\Delta R/R_{on}$ vs. t_{tot} in RNO/LSMO channels, with the layer thickness in the unit of uc labeled. (f) Maximum $\Delta R/R_{on}$ vs. $t_{channel}$ for various correlated oxide channels. Inset: $\Delta R/R_{on}$ vs. V_g switching hysteresis taken on a PZT/2.5 uc LNO/2 uc LSMO sample. Adapted from ref. 41 with permission from Springer Nature, copyright 2023.

For the bilayer channels, the presence of LSMO further provides an extended screening layer for minimizing the depolarization field in PZT, yielding excellent retention compared with the single-layer devices (Fig. 10(c) and (d)). For the 3 uc LNO/2 uc LSMO channel, $r_{off/on}$ stabilizes at 55% of the initial value after a few hours (Fig. 11(a)).[41] The cycling behavior shows a characteristic three-stage fatigue behavior consistent with previous reports of PZT thin films:[117] (I) slow fatigue stage until 10^6 cycles, (II) logarithmic stage until 10^8 cycles, and (III) saturated stage settling at 76% of the initial value until 10^{10} cycles (Fig. 11(b)). The high frequency conductivity has been investigated by microwave impedance microscopy (MIM) (Fig. 11(c)), which shows that the on–off ratio is stable up to

1 GHz (Fig. 11(d)), confirming that the resistance switching originates from the modulation of carrier density rather than ionic defects (e.g., oxygen vacancies).[118] The high on–off ratio,[41] excellent retention and endurance,[41] fast switching,[113] robust high frequency response,[118] and potential for constructing epitaxial three-dimensional architectures[119] make the Mott FeFETs highly competitive for developing nonvolatile memories and neuromorphic computing, which can be potentially integrated with the main stream Si technology.[30–32]

4.1.3 All-oxide ferroelectric tunnel junctions with correlated oxide electrodes. The device concept of ferroelectric tunnel junction has been intensively investigated in recent years for developing energy-efficient electronics and neuromorphic
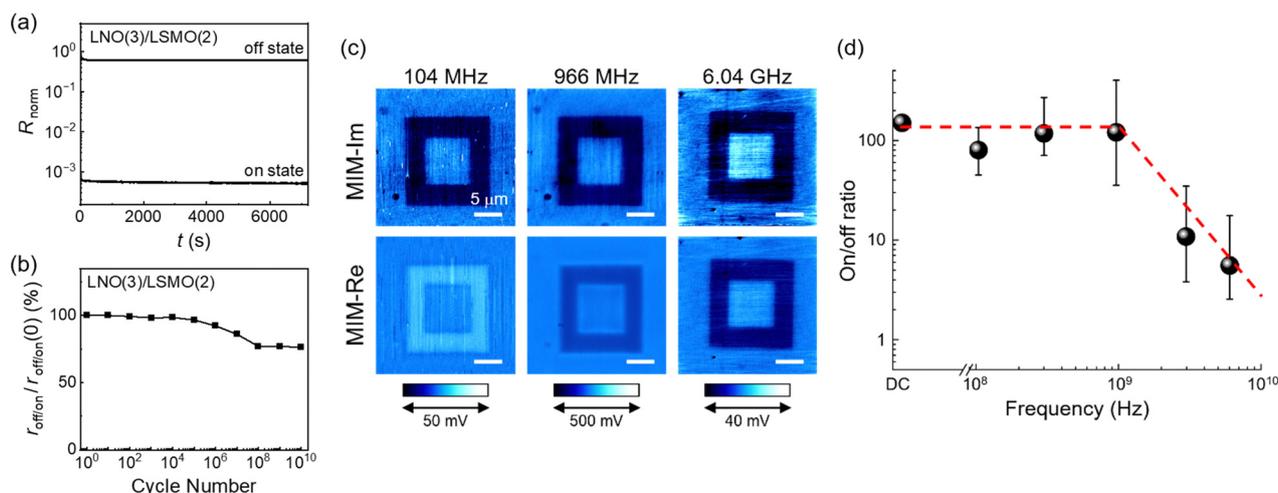

Fig. 11 Room temperature performance of RNiO$_3$-based Mott FeFETs. (a) Retention and (b) cycling behaviors of a PZT/3 uc LNO/2 uc LSMO sample. Reproduced from ref. 41 with permission from Springer Nature, copyright 2023. (c) MIM imaginary (top) and real (bottom) signal images (bottom) of a 3 uc LNO/2 uc LSMO channel underneath square domains of PZT, and (d) the extracted conductance on/off ratio vs. imaging frequency. Adapted from ref. 118 with permission from AIP Publishing, copyright 2024.

computing.[6,120] For FTJs adopting electrodes with different screening capacities, switching the ferroelectric polarization modifies the tunneling potential profile, leading to a nonvolatile electroresistance (ER).[121,122] Epitaxial complex oxide heterostructures are a promising platform for developing FTJs due to the high quality interface, precise thickness control, scalable growth, and high switching speed.[123] Critical considerations for designing all-oxide FTJs include the room temperature ER, which calls for strong potential asymmetry, and the retention behavior, as the depolarization effect is more severe in ultrathin ferroelectric oxide tunnel barriers close to the finite size limit. While semiconducting electrodes[124] or ferroelectric/dielectric composite tunnel barriers[125] have been adopted to produce high ER, these material choices provide insufficient interfacial screening and can lead to poor retention due to the strong depolarization effect. Working with correlated oxide electrodes with high carrier density can effectively minimize the depolarization field. The ER of correlated oxide-based FTJs, however, is often small due to the similar screening capacity of different correlated oxides.

In ref. 99, Zhang *et al.* showed that a giant room temperature ER can be achieved in all-oxide FTJs by pairing a correlated metal LaNiO$_3$ with a narrow bandgap Mott insulator Sr$_3$Ir$_2$O$_7$ as electrodes (Fig. 12(a) and (b)). Switching the PZT polarization in LaNiO$_3$/PZT/Sr$_3$Ir$_2$O$_7$ FTJs into the P_{up} and P_{down} states results in high (I_{on}) and low (I_{off}) tunneling current, respectively. At room temperature, the ER, defined as ($I_{on} - I_{off}$)/I_{off}, is 6500% (1000%) for the FTJ with 4 nm (2.8 nm) PZT barrier (Fig. 12(c)), which is one to three orders of magnitude higher than those of all-oxide FTJs with correlated oxide electrodes and similar tunnel barrier configurations (Fig. 12(d)).[126–128] The giant enhancement has been attributed to the polarization induced metal–insulator transition in the interfacial Sr$_3$Ir$_2$O$_7$, which is feasible as Sr$_3$Ir$_2$O$_7$ is a narrow-gap Mott insulator with a

bandgap of about 0.1 eV,[129] leading to a highly asymmetric tunnel barrier energy profile for the P_{up} and P_{down} states (Fig. 12(e)). Moreover, Sr$_3$Ir$_2$O$_7$ exhibit moderate conductivity even in the insulating state, effectively reducing the depolarization field. For the FTJ with thicker (4 nm) barrier, no apparent relaxation has been observed in the tunneling conductance. At 100 K, the ER ratio increases to 1.62×10^5% (1.46×10^5%) for the FTJ with 4 nm (2.8 nm) PZT barrier (Fig. 12(c)), which has been attributed to the pyroelectric increase of ferroelectric polarization.[23] The larger coercive field and the suppressed on-state relaxation behavior even for the FTJ with ultrathin (2.8 nm) barrier are consistent with the suppressed domain wall depinning of PZT at low temperature.[48] The giant ER, nonvolatile reversible switching, and superb retention make the all-oxide FTJs with narrow bandgap Mott electrodes highly competitive for nonvolatile memory and neuromorphic computing applications.

4.1.4 Ferroelectric polarization control of magnetism. For correlated oxides, the electronic state is closely intertwined with magnetism. The ferroelectric field effect is a powerful tool for identifying the individual contributions of charge, lattice, and defect effects in determining the magnetic properties.[10,11] It has been shown that in epitaxial ferroelectric/correlated oxide heterostructures, the polarization control of carrier density in the ultrathin correlated oxide channel can lead to the modulation of the magnetic T_C and magnetic anisotropy,[92,100,130,131] which has been assessed by magneto-optics,[132] X-ray spectroscopy,[131,133] and magnetotransport studies.[15,92,100,130] The nonvolatile voltage-control of magnetism has been extensively studied for developing energy-efficient spintronics.[4,12,13]

In ref. 100, Rajapitamahuni *et al.* demonstrated the manipulation of magnetic anisotropy energy (MAE) in 4 nm La$_{0.8}$Sr$_{0.2}$MnO$_3$ on (001) SrTiO$_3$ *via* the ferroelectric field effect.
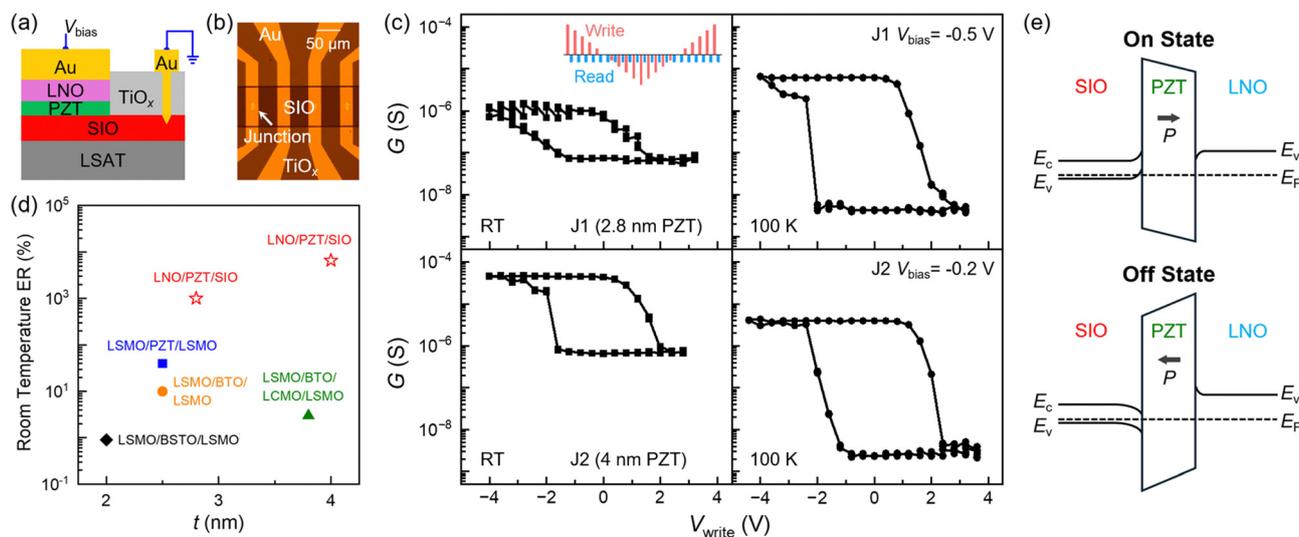

Fig. 12 Fabrication and characterization of LaNiO$_3$/PZT/Sr$_3$Ir$_2$O$_7$ FTJs. (a) Device schematic. SIO: Sr$_3$Ir$_2$O$_7$. (b) Optical image of a sample patterned with four tunnel junctions. (c) Tunneling conductance G *vs.* writing voltage V_{write} at room temperature and 100 K for FTJs with 2.8 nm and 4 nm PZT barriers. (d) Room temperature ER *vs.* tunnel barrier thickness t for various all-oxide FTJs.[126–128] LCMO: (La,Ca)MnO$_3$. BTO: BaTiO$_3$. BSTO: (Ba,Sr)TiO$_3$. (e) Schematic band diagrams for the on and off states. Adapted from ref. 99 with permission from AIP Publishing, copyright 2024.

For nanoscale magnetic materials, where the sample volume is too small for detection with conventional magnetometry, the anisotropic magnetoresistance (AMR) and planar Hall effect (PHE) are sensitive tools for assessing the magnetic state.[134,135] In the coherent rotation model, the PHE and AMR resistance are given by:[135]

$$R_{PHE} = (R_\parallel - R_\perp)\sin\varphi\cos\varphi,$$

$$R_{AMR} = R_\perp + (R_\parallel - R_\perp)\cos^2\varphi. \quad (1)$$

Here, φ is the angle between the current and in-plane magnetization (Fig. 13(a)). Fig. 13(b) shows R_{AMR} and R_{PHE} taken on a PZT/4 nm La$_{0.8}$Sr$_{0.2}$MnO$_3$ heterostructure at 125 K as a function of the angle θ between current and the in-plane magnetic field. At high magnetic fields, the magnetization follows the field direction ($\varphi \approx \theta$), and R_{AMR} and R_{PHE} exhibit sinusoidal θ-dependence. At low magnetic fields, the MAE dominates the Zeeman energy, and the magnetization is pinned to the easy axis ([110] or [1$\bar{1}$0]). As a result, R_{PHE} exhibits two distinct resistance states with sharp switching behavior. The switching hysteresis between these two R_{PHE} states in magnetic fields closely resembles those of MRAM (Fig. 13(c)), offering a simple material design for magnetic memories based on a single-layer LSMO thin film.[135]

Switching the ferroelectric polarization not only shifts the T_C of LSMO (Fig. 8(b)),[12,132,133] but also modulates the AMR and PHE.[92,100,130] For the 4 nm La$_{0.8}$Sr$_{0.2}$MnO$_3$, the resistance ratio between the two polarization states for R_{AMR} and R_{PHE} is about 3.5 ± 0.2 and independent of the magnetic field (Fig. 13(b)). The larger switching fields for R_{PHE} in the P_{up} state suggest the

change in MAE (Fig. 13(c)). The MAE has been quantified by analyzing the angular dependence of R_{PHE}: the anisotropy field marks the critical magnetic field for aligning the magnetization to the field direction ($\varphi \approx \theta$).[137] Fig. 13(d) shows the deduced E_{MAE} of the La$_{0.8}$Sr$_{0.2}$MnO$_3$ channel for both polarization states of PZT as well as single-layer La$_{1-x}$Sr$_x$MnO$_3$ with $x = 0.2$ and 0.33. The field effect induced change of MAE agrees well with the doping induced modulation of d-orbital occupancy predicted via density functional theory (DFT) calculations. In contrast, the change in MAE for the chemically doped sample is smaller than that expected from the doping variation, which can be attributed to the chemical substitution induced strain effect: La$_{1-x}$Sr$_x$MnO$_3$ with larger x possesses a smaller lattice constant and thus is subjected to larger tensile strain on SrTiO$_3$,[101] which suppresses the in-plane MAE.[100] The strain effect on MAE has been leveraged to design the magnetocrystalline anisotropy in nanostructured La$_{0.67}$Sr$_{0.33}$MnO$_3$ thin films, where the top layers are patterned into periodic nano-stripes. The depth modulated regions host a large strain gradient, yielding giant enhancement of uniaxial magnetocrystalline anisotropy and multilevel resistance switching (Fig. 13(e)).[136,137] It is conceivable that combining the ferroelectric field effect with the nanostructured LSMO thin films can lead to novel magnetic memory devices with multilevel information storage unit and voltage-controlled switching.

4.2 Ferroelectric–dielectric oxide heterostructures

4.2.1 Ferroelectric-to-dielectric transition. For ferroelectrics, the free energy vs. polarization P exhibits a double well profile, where the ground states settle at a finite remnant
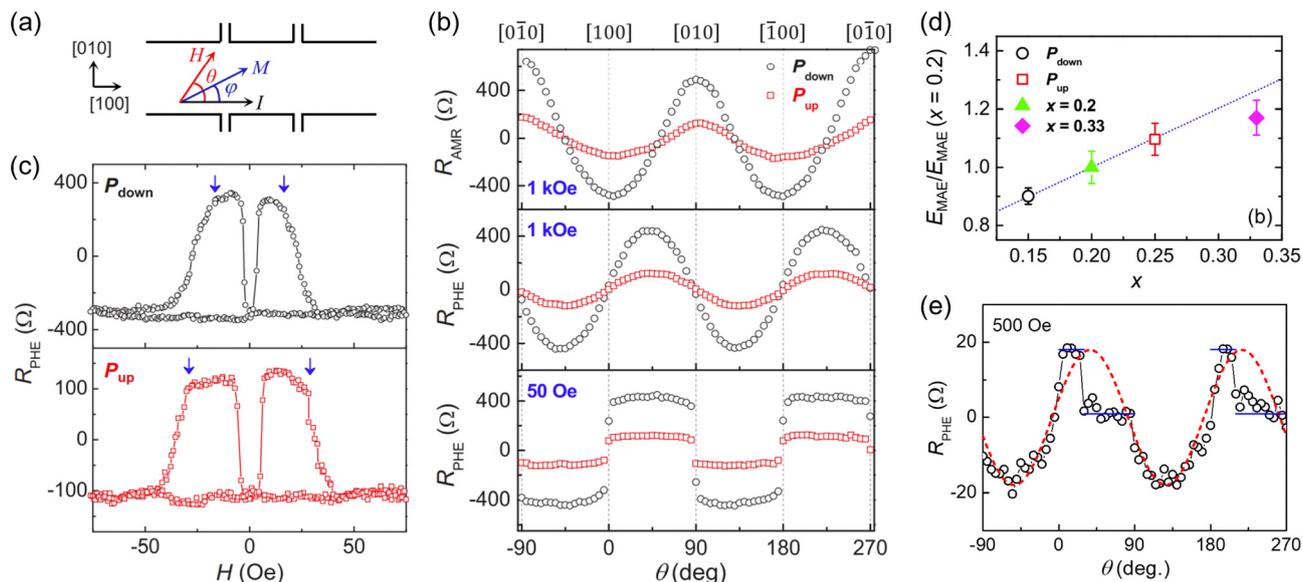

Fig. 13 Effects of the field effect doping and strain on magnetic anisotropy in LSMO. (a)–(d) AMR and PHE in PZT/4 nm La$_{0.8}$Sr$_{0.2}$MnO$_3$ on STO. (a) Schematic measurement geometry. (b) θ-dependence of R_{AMR} and R_{PHE} at different magnetic fields. (c) $R_{PHE}(H)$ at 125 K for both polarization states of PZT. (d) Normalized MAE vs. hole doping level x extracted from PZT/La$_{0.8}$Sr$_{0.2}$MnO$_3$ (open symbols) and single-layer La$_{1-x}$Sr$_x$MnO$_3$ thin films (solid symbols). The dotted line illustrates the DFT modeled doping dependence. Adopted from ref. 100 with permission from American Physical Society, copyright 2019. (e) R_{PHE} vs. θ at 100 K taken on a 6 nm LSMO with half of the channel patterned into nano-stripes (250 nm width, 1.2 nm depth) perpendicular to I. The red dashed line is a fit to eqn (1). The blue solid lines illustrate the pinning of R_{PHE}. Reproduced from ref. 136 with permission from the Society of Photo-Optical Instrumentation Engineers (SPIE), copyright 2018.

polarization P_r (Fig. 14(a)). Polarization switching between different orientations requires an external field higher than the coercive field E_c, yielding a P–E hysteresis loop (Fig. 14(b)). When a ferroelectric is interfaced with a dielectric layer, the matching of displacement field results in strong depolarization, which reduces the double well energy and net polarization in the ferroelectric layer. By tuning the thickness ratio between the ferroelectric (FE) and dielectric (DE) layers, it is possible to induce a ferroelectric-to-dielectric phase transition in the FE/DE stack structure. In ref. 39, Hao *et al.* investigated the FE-to-DE transition in a series of epitaxial PZT/STO heterostructures with a total thickness of 100 nm by tuning the layer thickness ratio $r = t_{PZT}/t_{STO}$ (Fig. 14(c)). The P–V loops show that the remanent polarization P_r of the PZT/STO stack decreases with decreasing r (Fig. 14(d)). Single-layer PZT exhibits a butterfly-shape of capacitance *vs.* V_{bias} (C–V) loop (Fig. 14(e)). In PZT/STO stacks with high PZT content, the butterfly first broadens, consistent with the higher E_c observed in the P–V loop (Fig. 14(d)), which can be attributed to the partial voltage drop across STO. With r further decreasing, the switching hysteresis in P–E and C–V loops gradually closes. There is a shoulder-like feature in the hysteresis for heterostructures with $r = 9$ and 6,

reflecting the competition between the fast nuclear and growth process and the slower DW propagation upon emergence of a multidomain state.[138]

Fig. 15(a) and (b) summarizes the P_r (a) and effective dielectric constant $\varepsilon_{eff} = C[(t_{PZT} + t_{STO})/\varepsilon_0 A]$ (b) measured for PZT/STO and STO/PZT stacks with different r values.[39] Sharp quenching of P_r occurs at $r = 7$–8, indicating a FE-to-DE phase transition. Such a transition can be well described by the Landau–Ginzburg–Devonshire (LGD) theory incorporating domain formation (Fig. 14(c)), where the free energy density of the PZT/STO stack (Fig. 15(c)) is expressed as:

$$g(P, V) = \frac{t_{PZT}}{t_{PZT} + t_{STO}} \times \left[\alpha P^2 + \beta P^4 + \gamma P^6 + k(\nabla P)^2\right]$$
$$+ \frac{t_{STO}}{t_{PZT} + t_{STO}} \times \frac{D^2}{2\varepsilon_{STO}\varepsilon_0} - DE. \quad (2)$$

Here α, β, and γ are the Landau coefficients, which can be
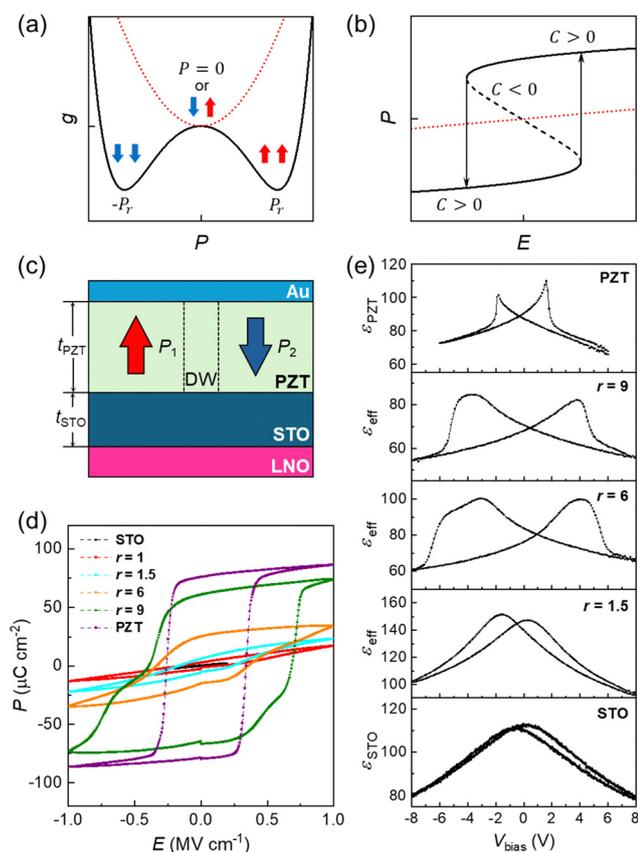

Fig. 14 FE-to-DE transition in PZT/STO stacks. (a) and (b) Schematics of ferroelectric free energy density g *vs.* P (a) and P–E loop (b). The dotted lines represent the dielectric responses. (c) Schematic of a PZT/STO stack hosting a DW. (d) P–E loops and (e) effective dielectric constant *vs.* V_{bias} for PZT/STO stacks with different PZT/STO thickness ratios r. Reproduced from ref. 39 with permission from American Physical Society, copyright 2021.
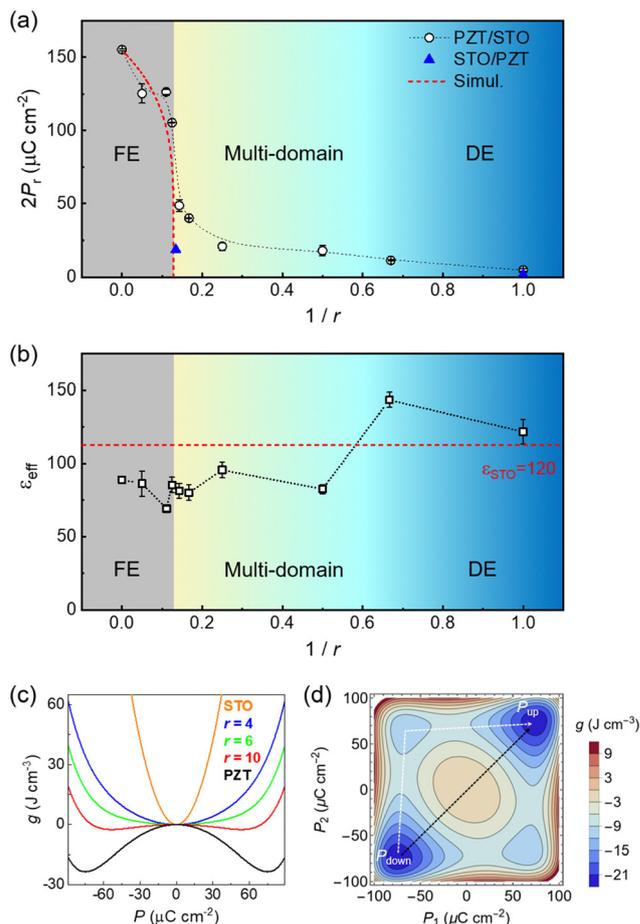

Fig. 15 Characterization and modeling of PZT/STO stacks. (a) $2P_r$ *vs.* $1/r$ for PZT/STO (open symbols) and STO/PZT (solid symbol) stacks. The dashed line is the simulation result using a single-domain model. (b) ε_{eff} *vs.* $1/r$ for PZT/STO stacks. The dashed line indicates the dielectric constant for single-layer STO. (c) Simulated $g(P)$ for PZT/STO stacks with different r within the single-domain model. Adapted from ref. 39 with permission from American Physical Society, copyright 2021. (d) Simulated free energy contour plot of PZT hosting a DW as functions of P_1 and P_2. Reproduced from ref. 139 with permission.

extracted by fitting the P–E loop of PZT (Fig. 4(a)), k is the DW coupling constant, and D is the displacement field. The three terms in eqn (2) describe the contributions from the ferroelectric layer, the dielectric layer, and the electrostatic energy associated with the applied electric field, respectively.

Under the single-domain conditions ($D \approx P$ and $\nabla P = 0$), this model predicts a FE–DE transition at a critical thickness ratio $r_c = 7.8$, where P_r vanishes (Fig. 15(a)) and the free energy evolves from a double-well to a single energy minimum at $P = 0$ (Fig. 15(c)). Even though the simulated r_c agrees well with the experimental result (Fig. 15(a)), the residue hysteresis window and gradual decrease of P_r in PZT/STO stacks beyond r_c cannot be captured by the single-domain model.[39] The possible explanations include the contribution of STO, an incipient ferroelectric with nonzero P_r at high bias,[82] and the emergence of a multidomain state between the FE and DE phases.[19,138,140] Fig. 15(d) shows the simulated energy profile of PZT hosting a 180° DW between two polar domains with independent polarizations of P_1 and P_2 based on eqn (2).[139] Switching between the fully polarized single-domain states (two diagonal corners: $P_1 = P_2 = \pm P_r$) can either go through the dielectric state (center point: $P_1 = P_2 = 0$) or detour to the off-diagonal local energy minima, which correspond to the multidomain state (both P_1 and P_2 are finite). For the PZT/STO stack, the off-diagonal points can evolve into global energy minimum in a certain range of r, preferring the multidomain state rather than the dielectric state. The slow DW motion during polarization switching results in residual P_r. This multidomain state can be suppressed by further reducing the ferroelectric content, and the PZT/STO stack eventually settles at a nonpolarized, dielectric state with entirely quenched P_r.

4.2.2 Transient negative capacitance effect. For ferroelectrics, the free energy profile in the vicinity of $P = 0$ exhibits a negative curvature (Fig. 14(a) and 15(c)), which corresponds to a negative slope in the P–E relation (Fig. 14(b)). It can be characterized as an effective negative capacitance. The NC effect has garnered intensive research interest as it can be leveraged to anchor steep-slope switching, or sub-60 mV decade^{-1} room temperature subthreshold swing (SS), in transistors adopting a ferroelectric gate.[141,142] As shown in Fig. 15(b), for the PZT/STO stacks with certain layer thickness ratios (e.g., r = 1.5 and 1), the ε_{eff} values become higher than those of single-layer PZT ($\varepsilon_{PZT} \approx 90$) and STO ($\varepsilon_{STO} \approx 120$),[39] suggesting the existence of a steady-state NC mode in the ferroelectric layer. The negative curvature of the ferroelectric free energy has previously been assessed by evaluating the charge dynamics during polarization switching in ferroelectric capacitors, known as the transient NC effect.[143–145]

Hao et al. investigated the transient NC effect in the PZT/STO stacks.[39] As shown in Fig. 16(a), when a square wave of source voltage (V_s) larger than the coercive voltage is applied to the PZT/STO stack with r = 8, the voltage across the capacitor (V_{cap}) exhibits a prominent damping during the initial charging (Fig. 16(a) and (b)), the characteristic behavior of the transient NC effect. In the Q–V curves deduced by integrating the charging current, an S-shape emerges (Fig. 16(c)), which is the direct
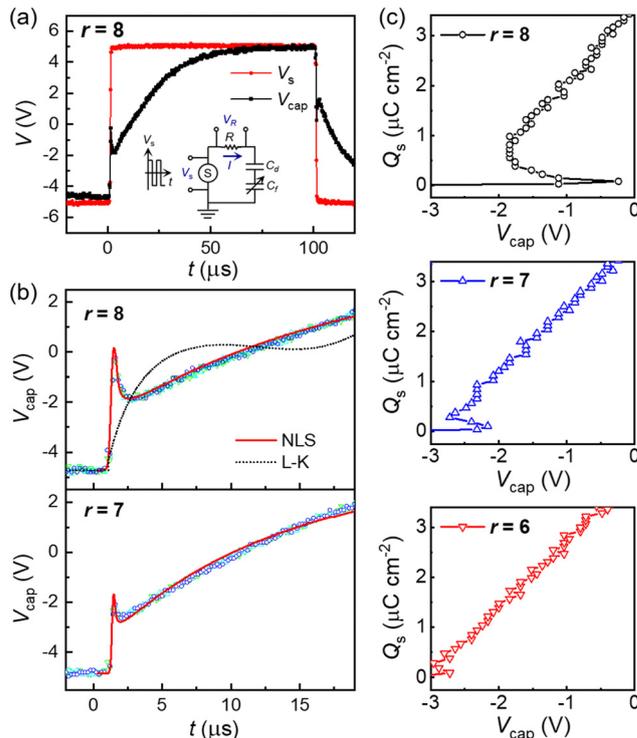

Fig. 16 Transient NC effect in PZT/STO stack capacitors. (a) Voltage across a PZT/STO capacitor with r = 8 (V_{cap}) upon applied square wave source voltage (V_s). Inset: Schematic experimental setup. (b) $V_{cap}(t)$ in the transient NC regime (open symbols) for the r = 8 and 7 samples with fits to the KAI/NLS model (solid line) and LK model (dotted line). (c) Q_s vs. V_{cap} in PZT/STO stacks with r = 8, 7, and 6. Adapted from ref. 39 with permission from American Physical Society, copyright 2021.

manifestation of the NC mode (Fig. 15(c)). The voltage damping behavior and S-shape in Q–V gradually diminish with increasing STO content, becoming barely visible in the r = 6 sample (Fig. 16(c)), which is consistent with its vanishing ferroelectric order (Fig. 15(c)).

As shown in Fig. 16(b), the transient NC behavior in the PZT/STO stack cannot be described by the Landau–Khalatnikov (LK) dissipative model based on single-domain polarization switching.[146] Instead, the nucleation-limited-switching (NLS) model can quantitatively describe the fast V_{cap} damping followed by slow recovery.[146,147] Phenomenologically, this model considers polarization switching involving multiple independent nucleation sites, where the domain growth is constrained by defect pinning and grain size. The polarization switching within a single-domain region is characterized by the Kolmogorov–Avrami–Ishinashi (KAI) factor $1 - \exp[-(t/t_0)^n]$, where t_0 characterizes the time scale of DW propagation between different nucleation regions. Modeling the transient NC behavior using the KAI/NLS model reveals a narrow distribution of t_0 for the r = 8 sample, consistent with the single-domain scenario, and a notably broader distribution of t_0 for the r = 7 sample.[39] The latter points to a multidomain state, where the DW motion is hindered by the formation of quasi-static, soft DWs, resulting in heterogeneous switching dynamics across different switching regions with a large variation in t_0. The emergence of the multi-

domain state can be utilized to anchor the steady-state NC effect, which is essential for the operation of NC-FETs, as illustrated in Section 5.1.3.

5. Ferroelectric oxide–2D van der Waals heterostructures

5.1 Ferroelectric field effect in van der Waals materials

5.1.1 Ferroelectric-gated van der Waals transistors. Compared with polymer and van der Waals ferroelectrics, the large polarization, high dielectric constant, and high T_C of ferroelectric oxides make them powerful gate materials for tuning the electronic and optical properties of 2D van der Waals materials, including graphene and transition metal dichalcogenides (TMDCs).[4,14] Combining the ferroelectric field effect with nanoscale domain control also enables local modulation of carrier densities, which can be utilized to impose the pn junction state and superlattice modulation.[23,57,148] On the other hand, the 2D material can serve as a sensitive tool to probe the polarization of ferroelectric thin films, which is challenging for conventional characterization methods due to the large leakage current. For example, Hall effect measurements have been conducted in monolayer (1L) graphene back-gated by $Ba_{0.6}Sr_{0.4}TiO_3$ (BSTO)[52,149] and PZT[23] thin films to examine the remnant polarization, coercive field, dielectric constant, and pyroelectric coefficients of the ferroelectric gates.

Fig. 17(a) shows the longitudinal resistivity ρ_{xx} vs. V_g at 2 K taken on a 1L graphene FET back-gated by a BSTO thin film, which exhibits switching hysteresis that is consistent with ferroelectric polarization doping.[149] The corresponding carrier

density has been deduced from Hall measurements, $n = 1/eR_H$, where R_H is the Hall coefficient (Fig. 17(b)). Beyond the hysteresis window, BSTO behaves as a typical high-κ dielectric, with low temperature κ close to 100. Due to the efficient dielectric screening, the ferroelectric-gated graphene FETs exhibit high mobilities,[49] with a field effect mobility of up to 23 000 cm^2 V^{-1} s^{-1} and nonvolatile modulation of the quantum Hall effect (Fig. 17(c) and (d)) observed in BSTO-gated 1L graphene.[52,149]

For 2D FETs back-gated by PZT and BSTO, the high temperature switching hysteresis is often opposite to that expected for ferroelectric polarization doping, known as an anti-hysteresis.[50,52,53] When the van der Waals layer is transferred on the ferroelectric oxide at temperatures below T_C, the bound charge on the ferroelectric surface is pre-screened by the ambient charged adsorbates[50] or surface defect states,[53] whose dynamic response to the applied electric field can over-screen the ferroelectric polarization and lead to the anti-hysteresis. To achieve appropriate switching hysteresis in 2D vdW FETs at room temperature, it is preferable to exploit high-temperature transfer above T_C[53] or work with a top-gate geometry. In ref. 28, Wu et al. fabricated few-layer MoS$_2$ FETs sandwiched between a SiO$_2$ back-gate and a PZT membrane top-gate (Fig. 17(e) and (f)), using conductive AFM to switch PZT's polarization. These devices exhibit nonvolatile modulation of the source–drain current (I_{ds}) that agrees with ferroelectric polarization switching, with a current on–off ratio of up to 2 × 10^5 and no apparent decay for 3 days at 300 K (Fig. 17(g)).

The ferroelectric oxides possess high dielectric constants (Fig. 14(e)), resulting in soft remote surface optical (RSO) phonon modes that can significantly impact the mobility of the 2D channel.[4,149–151] Fig. 18(a) shows $\rho_{xx}(T)$ at different
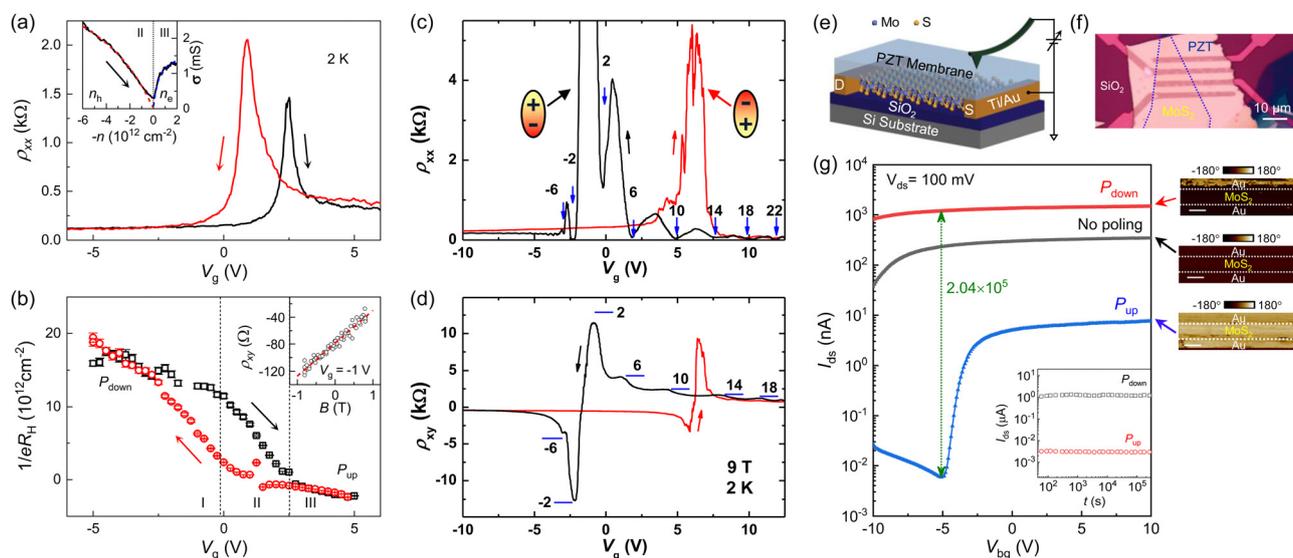

Fig. 17 Ferroelectric field effect in vdW FETs. (a)–(d) A 1L graphene FET with a BSTO back-gate. (a) $\rho_{xx}(V_g)$ and (inset) σ vs. $-n$ at 2 K. (b) $1/eR_H$ vs. V_g at 2 K. Inset: ρ_{xy} vs. B at $V_g = -1$ V for up-sweep. Adapted from ref. 149 with permission from AIP Publishing, copyright 2022. (c) ρ_{xx} and (d) ρ_{xy} vs. V_g at 2 K and 9 T. Reproduced from ref. 52 with permission from American Chemical Society, copyright 2013. (e)–(g) A few-layer MoS$_2$ FET with an SiO$_2$ back-gate and a PZT membrane top-gate. (e) Device schematic. (f) Optical device image. (g) I_{ds} vs. V_{bg} at 300 K for the no poling, P_{up}, and P_{down} states of the PZT top-gate. (insets) PFM images of PZT (right) and device retention for the P_{up} and P_{down} states of PZT (bottom). Adapted from ref. 28 with permission from American Chemical Society, copyright 2023.

carrier densities for a BSTO-gated 1L graphene FET.[149] Beyond the electron–hole puddle region, ρ_{xx} decreases upon lowering temperature due to phonon scattering, which can be well described by:

$$\rho_{xx}(T,n) = \rho_0(n) + \rho_{\text{LA}}(T,n) + \sum_i \rho_{\text{RSO}}^{(i)}(T,n). \quad (3)$$

Here $\rho_0(n)$ and $\rho_{\text{LA}}(T,n)$ account for the scattering contributions from impurities and intrinsic longitudinal acoustic (LA) phonons in graphene, respectively. The RSO phonon scattering is captured by $\rho_{\text{RSO}}^{(i)}(T,n) \propto (e^{\hbar\omega_i/k_{\text{B}}T} - 1)^{-1}$, with four RSO phonon modes $\hbar\omega_i = 15.1$ meV, 35.8 meV, 57.9 meV, and 86.8 meV for BSTO. Modeling using eqn (3) shows that $\rho_{xx}(T)$ is dominated by the LA phonon scattering below 80 K, yielding $\rho_{xx} \propto T$, and the RSO phonon scattering at high temperatures. Fig. 18(b) summarizes the 300 K mobility limits of BSTO-gated graphene imposed by various phonon modes, revealing the dominant role of the 35.8 meV RSO phonon mode. The overall mobility limit is about 3×10^4 cm^2 V^{-1} s^{-1} with weak density dependence, highly competitive compared to graphene gated by a conventional dielectric.[151] The ability to sustain high mobility in the 2D channel means it is possible to combine the ferroelectric field effect with nanoscale domain patterning for constructing programmable junction states and inducing superlattice modulation in a 2D channel. The presence of domains also introduces a new functional entity, the ferroelectric DW, as a control knob for designing 2D FETs. Next, we discuss two examples of ferroelectric oxide gate-enabled phenomena and device concepts in van der Waals materials.

5.1.2   1D Graphene superlattice with high transport anisotropy. For graphene subjected to one-dimensional Kronig–Penney (KP) potential (Fig. 19(a)), its band structure becomes highly anisotropic, with enhanced Klein tunneling along the superlattice vector direction ($\hat{s}$) and flattened band perpendicular to $\hat{s}$.[152,153] There is intensive research interest in realizing the 1D graphene superlattice (GSL) in the high KP potential

limit for achieving the electron lensing or supercollimation effects.[154,155] Experimentally, 1D KP potential has been imposed on graphene through modulated dielectric gates[156,157] and periodic domain patterning in ferroelectric gates.[23] In the former approach, the KP potential is limited by the gating capacity of the dielectrics, which is in the moderate regime (i.e., the scaled dimensionless KP potential up to $u = \dfrac{V_0 L}{\hbar v_{\text{F}}} \sim 9\pi$, with V_0 the KP barrier, L the superlattice period, and $v_{\text{F}} = 10^8$ cm s^{-1}, the Fermi velocity of graphene).[157] The dielectric thickness separating the gate electrode and graphene channel also leads to spatially dispersed potential profiles. In contrast, the ferroelectric domain approach can generate a step-like potential profile through direct contact with graphene, and the polarization doping of ferroelectric oxides such as PZT can be orders of magnitude higher than those of dielectric gates.

In ref. 23, Li et al. have achieved high KP potential ($u \sim 90\pi$) in 1D GSL by fabricating graphene FETs sandwiched between an h-BN top-gate and a PZT back-gate with prepatterned stripe domains of period $L = 200$–300 nm (Fig. 19(b)–(d)).[23] A polarization doping difference of up to 3×10^{13} cm^{-2} between the P_{up} and P_{down} states has been induced in graphene at low temperatures due to the pyroelectric effect, corresponding to a high KP potential of 0.9 eV. For the 1D GSL with $\hat{s}$ parallel to the current direction (denoted as R_{xx}), two satellite Dirac points emerge in $R_{\square}$ vs. electron doping induced by the top-gate (δn) (Fig. 19(e)), indicating the formation of higher-order bands due to superlattice Brillouin zone folding. In magnetic fields, R_{xx} develops into three sets of Landau fans, originating from the original Dirac point and two satellite Dirac points (Fig. 19(f)). For the 1D GSL with $\hat{s}$ perpendicular to the current direction (denoted as R_{yy}), $R_{\square}(\delta n)$ exhibits a single peak (Fig. 19(g)) and only one set of Landau fans (Fig. 19(h)), confirming the highly anisotropic magnetotransport properties of the 1D GSL.

For $V_0 = 0.9$ eV and $L = 200$ nm, the scaled dimensionless KP potential reaches $u = 90\pi$. The corresponding band structure exhibits a highly flattened band along k_y ($E = \pm\hbar v_{\text{F}}(k_x + 2N\pi/L)$) with strongly suppressed Fermi velocity $v_y \sim 0.01 \, v_{\text{F}}$ (Fig. 19(i)). Experimentally, the relation between the average carrier density interval between two consecutive Dirac points and the superlattice period can be described by: $\Delta n_{\text{DP}} = AL^\beta$, with $\beta = -1.18 \pm 0.06$ (Fig. 19(j)). This quasi-inverse relation is a hallmark of the 1D GSL in the high KP potential limit, and the proportionality constant $A = 2/a_0$ yields $a_0 = 2.40$ Å, which is in excellent agreement with the graphene lattice constant 2.46 Å.

5.1.3   Domain wall enabled 2D negative capacitance transistors. For semiconductor FETs, the gate voltage (V_g) required to change the channel source–drain current (I_d) by one order of magnitude, known as the subthreshold swing (SS), is given by: $\text{SS} = \left(1 + \dfrac{C_{\text{ch}}}{C_g}\right)\dfrac{k_{\text{B}}T}{q}\ln 10$, where C_{ch} and C_g are the channel and gate capacitance, respectively. For a conventional dielectric gate with positive capacitance, the Boltzmann statistics impose a fundamental limit of SS ≈ 60 mV decade^{-1} at 300 K. It has been proposed that the effective negative capacitance in a
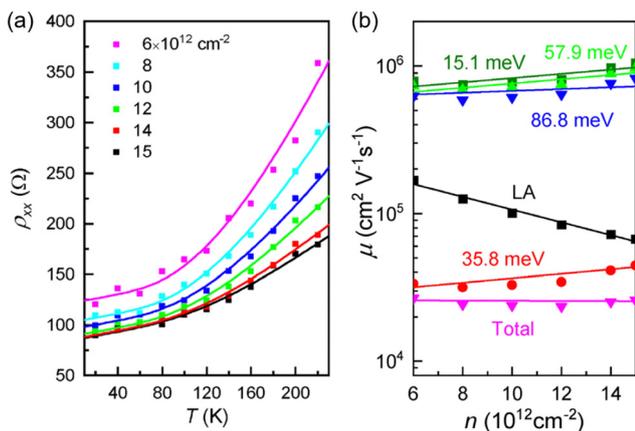

Fig. 18 Effect of RSO phonons on a BSTO-gated 1L graphene FET. (a) $\rho_{xx}(T)$ at various hole doping levels with fits to eqn (3). (b) Mobility limit at 300 K imposed by the LA and four RSO phonon modes and the overall contribution (total). Reproduced from ref. 149 with permission from AIP Publishing, copyright 2022.
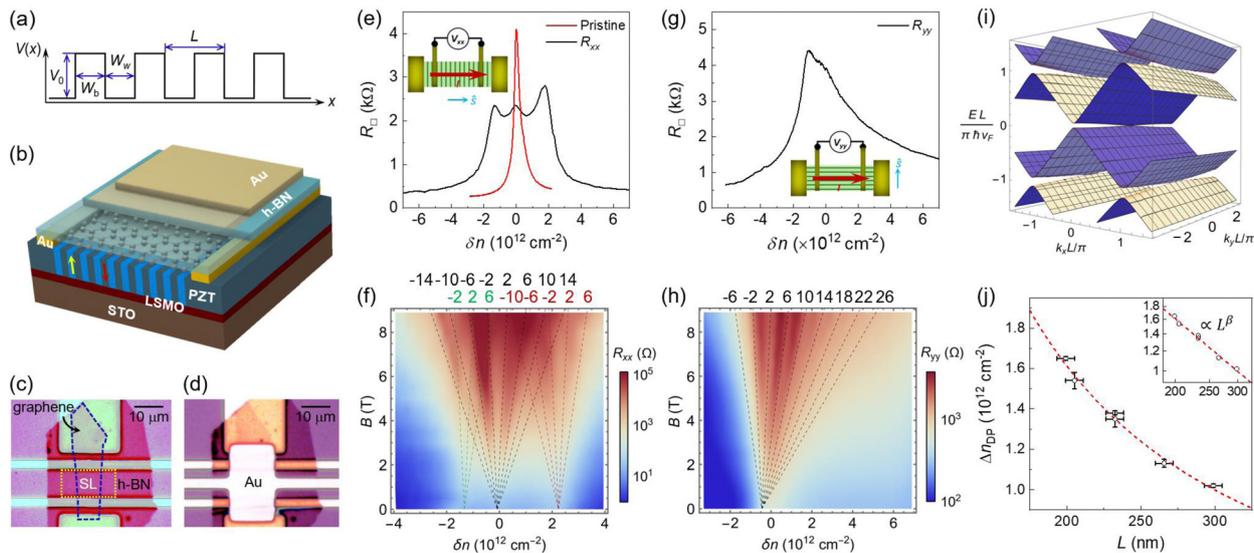
Fig. 19 PZT induced 1D graphene superlattice. (a) Schematic Kronig–Penney potential. (b) Sample schematic. (c) and (d) Optical images of an h-BN/ graphene/PZT sample before (c) and after (d) the deposition of the Au top-gate electrode. (e) $R_\square(\delta n)$ for pristine graphene and a 1D GSL sample (L = 205 nm) in the R_{xx} configuration, with (f) R_{xx} vs. δn and B. (g) $R_\square(\delta n)$ for a 1D GSL sample (L = 199 nm) in the R_{yy} configuration, with (h) R_{yy} vs. δn and B. The dashed lines illustrate the modeled Landau fans, with the filling factors labeled. (i) Calculated band structure for 1D GSL with scaled dimensionless KP potent u = 90π. (j) Δn_{DP} vs. L with a fit (dashed line) on linear and (inset) semi-log scales. Adapted from ref. 23 with permission from American Physical Society, copyright 2024.

ferroelectric gate close to P = 0 (Fig. 14(a)) can be exploited to achieve steep-slope switching, or sub-60 mV decade^{-1} SS at room temperature,[141,142] which can lead to energy-efficient logic devices with reduced operation voltage. Previous studies of NC-FETs have focused on utilizing a ferroelectric/dielectric stack gate to stabilize the steady-state NC mode,[7] and it is challenging to quench the ferroelectric hysteresis and achieve steep-slope switching at low gate-voltage. In ref. 55, Song *et al.* showed that it is possible to leverage the metastable polar state in ferroelectric DWs to enable steep-slope switching in a MoS$_2$ based NC-FET at ultra-low V_g towards hysteresis-free operation. Fig. 20(a) shows the 300 K transfer curves (I_d *vs.* V_g) of a few-layer (FL) MoS$_2$ FET back-gated by polycrystalline PbZr$_{0.35}$Ti$_{0.65}$O$_3$, which exhibits a current switching ratio of up to 8 × 10^6 over a small gate window of V_g = ±0.5 V that is below the coercive voltage V_c. The SS is below the Boltzmann limit over three decades of I_d for the forward V_g-sweep and over one decade of I_d for the backward V_g-sweep. The minimum SS for this device is SS$_{min}$ = 37 mV decade^{-1} and reaches SS$_{min}$ = 9.7 mV decade^{-1} in a bilayer MoS$_2$ FET at 300 K (Fig. 20(b)).

Compared with conventional NC-FETs, these MoS$_2$-based NC-FETs exploit a single-layer polycrystalline PZT gate. The steep-slope switching and nearly hysteresis-free behavior at low V_g have been consistently observed in multiple bilayer and FL devices at different temperatures (Fig. 20(c)) and remain stable across different source–drain voltages and gate-voltage scan rates. The high I_{on}/I_{off} achieved over a small operation voltage window of ΔV_g = 0.75 V makes the device performance highly competitive compared with other MoS$_2$-based NC-FETs and FE-FETs (Fig. 20(d)).[158–168] This quasi-static NC mode has been attributed to the high density DWs in the polycrystalline

PZT back-gate. Force field simulation shows that frustrated dipoles with flux-closure-type chiral rotation within the PZT DW can be polarized at an electric field well below E_c. It results in an abrupt jump in local polarization (Fig. 20(e)), which can quantitatively account for the steep-slope switching in surface MoS$_2$ at V_g = −0.25 V. While the 180° DW in bulk PZT is known to be of Ising type with unit-cell-scale width,[169] it has been shown that the flux-closure-type DW emerges in the presence of strong depolarization field, *e.g.*, at the ferroelectric surfaces,[170] grain boundaries,[171] and ferroelectric/dielectric interfaces.[19,20]

The suppression of DW density at low bias voltage has been confirmed by PFM studies. Fig. 20(f) shows the lateral PFM (L-PFM) image of a polycrystalline PZT film, which hosts a high density of DWs at zero V_{bias}. The sample is subsequently imaged with progressively higher DC V_{bias} that is below V_c applied, which reveals a suppressed DW density with increasing V_{bias}. Studies of bilayer MoS$_2$ NC-FETs show that the SS$_{min}$ increases monotonically with increasing V_g-range (Fig. 20(g)), which correlates well with the reduced DW areal density, pointing to the critical role of the metastable polar state in the DW in stabilizing the NC effect.

5.2 Ferroelectric oxide interfaced with polar 2D materials

5.2.1 Nonlinear optical tuning effect in PZT/MoS$_2$ heterostructures. Despite the intensive studies of the heterostructures composed of ferroelectric oxides and 2D transition metal dichalcogenides, previous work has mostly focused on charge mediated interface effects, *i.e.*, ferroelectric field effect tuning of the electronic properties[4,14] and optical responses such as photoluminescence (PL) in 2D TMDCs.[24,45,46,172,173] The polar nature of ferroelectric oxides, on the other hand, can lead to a
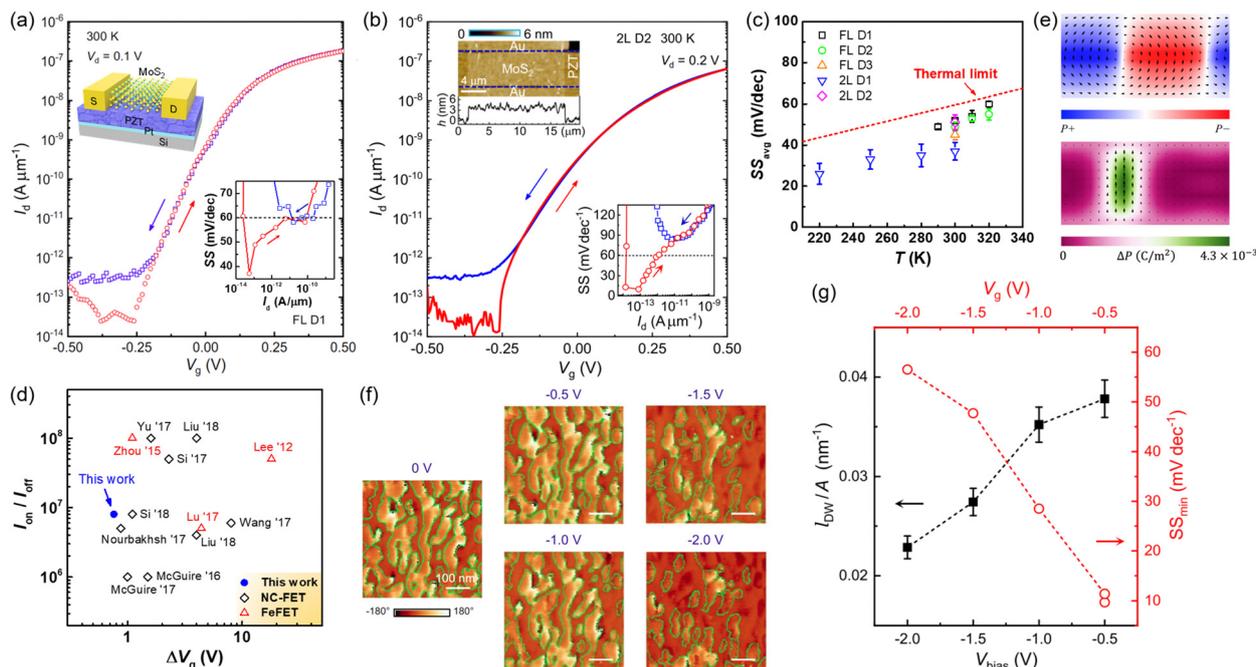
Fig. 20 DW enabled MoS$_2$ NC-FET gated by polycrystalline PbZr$_{0.35}$Ti$_{0.65}$O$_3$. (a) I_d vs. V_g of a few-layer MoS$_2$ FET at 300 K. Insets: Device schematic (top) and deduced SS vs. I_d (bottom). (b) I_d vs. V_g of a bilayer MoS$_2$ FET at 300 K. Insets: AFM image of the device (top) and deduced SS vs. I_d (bottom). (c) Average SS vs. T taken on 2 bilayer FETs and 3 FL FETs. The dashed lines in (a)–(c) indicate the Boltzmann limit. (d) Comparison of the room temperature current on/off ratio vs. operation voltage window ΔV_g for various NC-FETs and FeFETs with MoS$_2$ channels.[158–168] (e) Force field simulation of a flux-closure type domain structure (left) and the change of local polarization upon small bias below V_c (right) in PZT. (f) L-PFM images of a domain structure on PZT with progressively higher DC V_{bias}, with the DW position highlighted. (g) Areal density of DW length l_{DW}/A vs. V_{bias} extracted from (f) and SS$_{avg}$ vs. V_g-scan range taken on bilayer MoS$_2$ FETs. Adapted from ref. 55 with permission from Springer Nature, copyright 2022.

strong nonlinear optical signal such as second harmonic generation (SHG). For example, polarized SHG signals have been observed at DWs of PZT, which has been attributed to the chiral dipole rotation induced in-plane polarization at the DW surface.[174,175] An even stronger tuning effect of both the intensity and polarization of SHG signals has been demonstrated recently by interfacing PZT thin films and membranes

with a polar 2D TMDC, monolayer MoS$_2$ (Fig. 21(a)),[24,25] leveraging the interfacial coupling of the polar symmetry.

Fig. 21(b)–(d) shows a 1L MoS$_2$ flake transferred on a 50 nm PZT film pre-patterned with square domains, which reveals nonvolatile tuning of the PL signal. The intensity areal ratio between the negative trions (A$^-$) and neutral excitons (A^0), extracted by fitting the PL spectra (Fig. 21(d)), suggests that
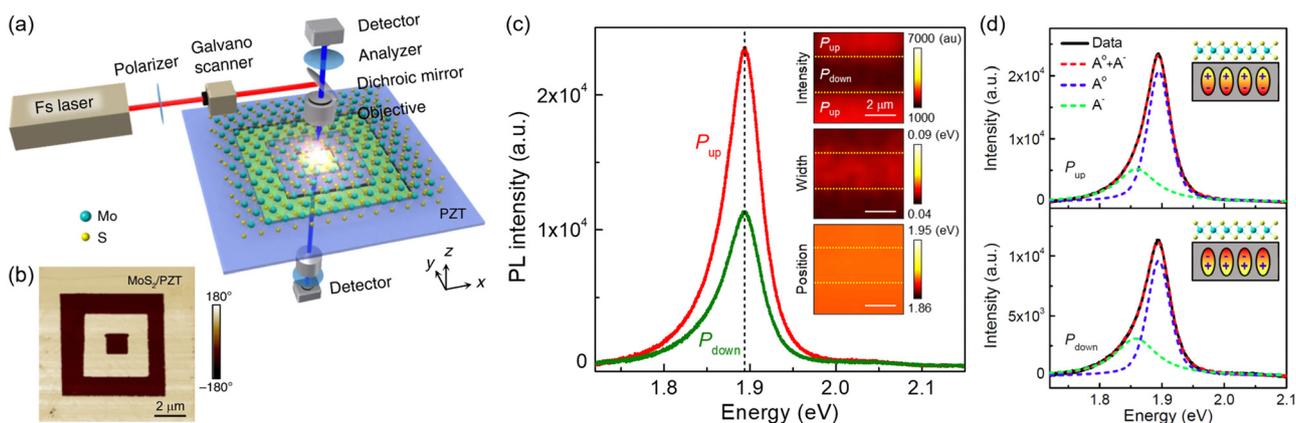

Fig. 21 Characterization of the PZT/1L MoS$_2$ heterostructure. (a) Schematic experimental setup. (b) PFM phase images of 1L MoS$_2$ transferred on a 50 nm PZT film prepatterned with square domains. (c) Room temperature PL spectra of 1L MoS$_2$ on the P_{up} and P_{down} domains shown in (b). Inset: PL mapping of the peak intensity (upper), width (middle), and position (lower) of 1L MoS$_2$ on P_{up} and P_{down} domains of PZT, with DW positions marked. (d) Fits to the PL spectra revealing the modulation of neutral excitons (A^0) and negative trions (A$^-$). Adapted from ref. 24 with permission from Springer Nature, copyright 2020.

the induced doping is dominated by the interfacial screening charge rather than ferroelectric polarization.[24] For (001) PZT thin films, normal-incidence light yields prominent SHG signals at the DW regions (Fig. 22(a)).[24] The light polarization of the SHG signal is perpendicular to the DW, which points to the presence of in-plane polarization at the Néel-type DWs, consistent with previous reports.[174,175] For 1L MoS_2/PZT heterostructures, there is a strong filtering effect of the SHG signal that depends on the relative alignment of polar axes as well as the measurement geometry.

Fig. 22(b) shows the SHG mapping of a 1L MoS_2/PZT heterostructure, where one of the polar axes of MoS_2 is aligned with the vertical DWs. In the reflected mode (R-SHG), the SHG signal is modulated at the DWs, remaining unchanged at the polar domains. The SHG signal on the horizental DWs shows alternating enhancement and suppression in intensity, which reflects the alignment between the polar axis of MoS_2 and the in-plane polarization of DW. DFT calculation shows that the in-plane polarization of a flux-closure type DW in PZT (Fig. 22(c)) is comparable with that of 1L MoS_2.[24] Combining these two can lead to about four times of the SHG intensity when the two polar axes are aligned and close to zero SHG intensity when they are anti-aligned (Fig. 22(d)).[24] The SHG signal on the the vertical DWs, on the other hand, cannot be differentiated from the background MoS_2, as the two polar axes are orthogonal to each other. The 1L MoS_2 can thus serve as an atomic-scale polarizer that can modulate the strength of the SHG signal based on its polar alignment with the DW. The modulation of the SHG strength and polarization can be quantitatively modeled using the nonlinear electromagnetic theory considering the coupling of second-order nonlinear optical susceptibility

tensors for MoS_2 and PZT DW. As shown in Fig. 22(e)–(h), both the amplitude and polarization of the SHG signal can be tuned by varying the angle between the polar axes of MoS_2 and PZT DW, which have been well captured by theoretical modeling.[25]

In the transmitted mode (T-SHG) for 1L MoS_2 on top of PZT thin films (MoS_2/PZT), the polar domain also exerts a strong tuning effect on the SHG signal (Fig. 23(a)). A similar effect has been observed in R-SHG for reversed sample geometry (PZT/MoS_2), *i.e.*, with 1L MoS_2 underneath a PZT membrane (Fig. 23(b)). The coupling with the PZT polar domain leads to three-fold polarization of the SHG signal, or C_{3v} symmetry, with the intensity peaking along the zig-zag directions of MoS_2 (Fig. 23(c)–(h)). This is in sharp contrast to the C_{6h} symmetry observed in standalone MoS_2[176] and C_{2v} symmetry observed in R-SHG of 1L MoS_2/PZT heterostructures (Fig. 22(h)), which can be well explained by considering the coupling of second-order nonlinear optical susceptibility tensors for MoS_2 and PZT (Fig. 23(e) and (h)).[25] For the PZT/MoS_2 geometry, the domain structure in the top PZT membrane is reconfigurable, facilitating *in operando* device operation.

5.2.2 Enhanced polar alignment in van der Waals ferroelectrics.
In addition to the coupling of polar symmetry, the interfacial synergy between the polar vdW materials and ferroelectric oxides can also be mediated by lattice. In ref. 22, Wang *et al.* reported controlled domain formation, enhanced ferroelectricity, and tunable piezoelectricity in thin $CuInP_2S_6$ (CIPS) flakes interfaced with PZT (Fig. 24(a)). The vdW ferroelectric CIPS has attracted intensive research interest in recent years due to large bandgap,[177] large out-of-plane polarization,[178] above room temperature T_C,[179] and stackable nature with other 2D vdW materials.[14] Its unconventional quadruple energy
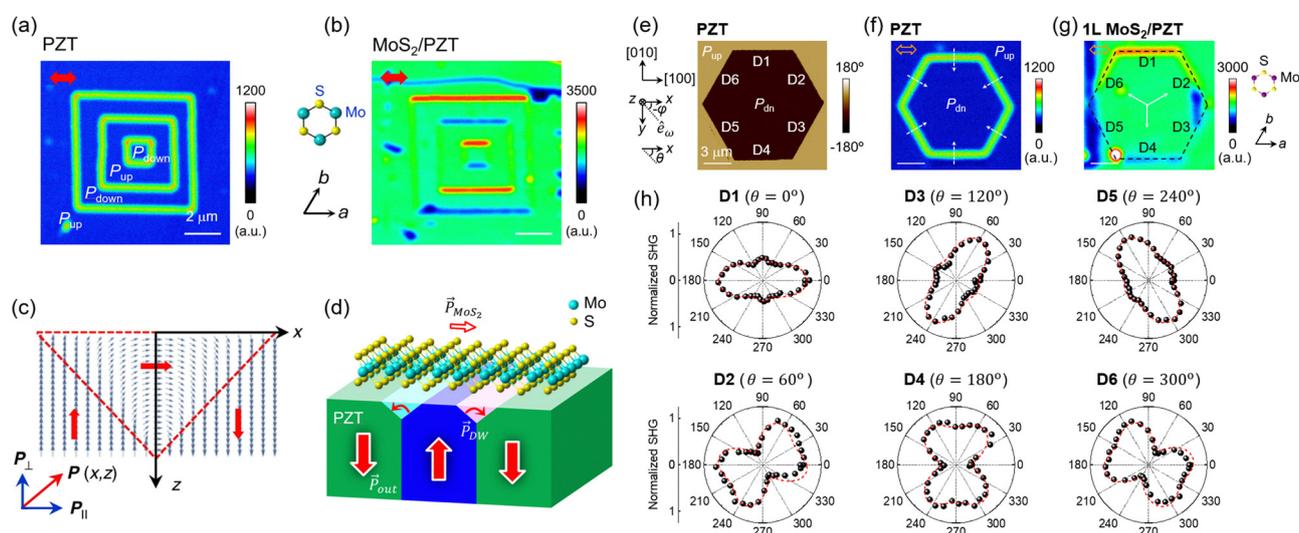

Fig. 22 DW filtering of SHG signals at 1L MoS_2/PZT interfaces. (a) R-SHG mapping of a domain structure on PZT with no analyzer applied before (a) and after (b) the transfer of 1L MoS_2 on top. (c) Schematic of a flux-closure type polar rotation at the surface of a 180° DW. (d) Schematic of the polar alignment at a 1L MoS_2/PZT interface. The arrows mark the local polarization directions. Reproduced from ref. 24 with permission from Springer Nature, copyright 2020. (e) PFM phase image and (f) R-SHG mapping of a hexagonal domain on bare PZT, and (g) R-SHG mapping after a 1L MoS_2 transferred on top. The open arrows show the direction of the incident light polarization. The dashed (solid) arrows mark the polarization directions of the DWs (MoS_2). (h) Polar plots of normalized R-SHG intensity *vs.* ϕ taken at different DWs in (g) with fits to nonlinear electromagnetic theory (dashed lines). Reproduced from ref. 25 with permission from Wiley-VCH GmbH, copyright 2022.
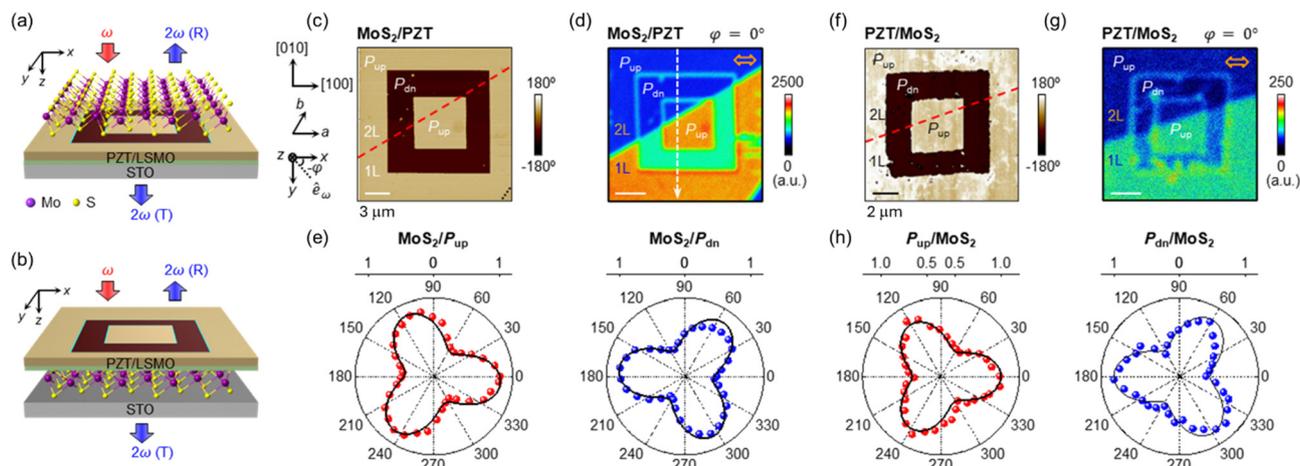
Fig. 23 Ferroelectric domain control of SHG signals. (a) Schematic of a 1L MoS_2/PZT thin film. (b) Schematic of PZT membrane/1L MoS_2. (c)–(e) T-SHG studies of MoS_2/PZT. (c) PFM phase image and (d) T-SHG mapping of a domain structure on MoS_2/PZT. The excitation laser power is 30 mW. (e) Polar plots of normalized T-SHG intensity *vs.* ϕ taken on the P_{up} and P_{down} domains in (d) with fits (solid lines). (f)–(h) R-SHG studies of PZT membrane/MoS_2. (f) PFM phase image and (g) R-SHG mapping of a domain structure on PZT/MoS_2. The excitation laser power is 7 mW. (h) Polar plots of normalized R-SHG intensity *vs.* ϕ taken on the P_{up} and P_{down} domains in (g) with fits (solid lines). Reproduced from ref. 25 with permission from Wiley-VCH GmbH, copyright 2022.

well[180] also leads to negative piezoelectricity[178] and inter-correlated out-of-plane/in-plane polarization switching.[181] Due to its high ionic conductivity,[182] it is challenging to have an electric field well confined at the nanoscale in CIPS, which leads to diffusive DWs. As shown in Fig. 24(b), for 13–14 nm CIPS flakes on PZT, the polar domains fully conform to those prepatterned on PZT, in sharp contrast to the spontaneously

formed small domains for CIPS of the same thickness on Si and Au base layers. The enhanced polar alignment only occurs in thin CIPS flakes, *i.e.*, with thickness below 25 nm (Fig. 24(c)). In this region, the flake on PZT also exhibits an enhanced, positive piezoelectric coefficient d_{33}^{CIPS}, in contrast to the negative d_{33}^{CIPS} for flakes on Si and Au (Fig. 24(d)), with the value increasing substantially with reducing CIPS thickness (Fig. 24(e)).
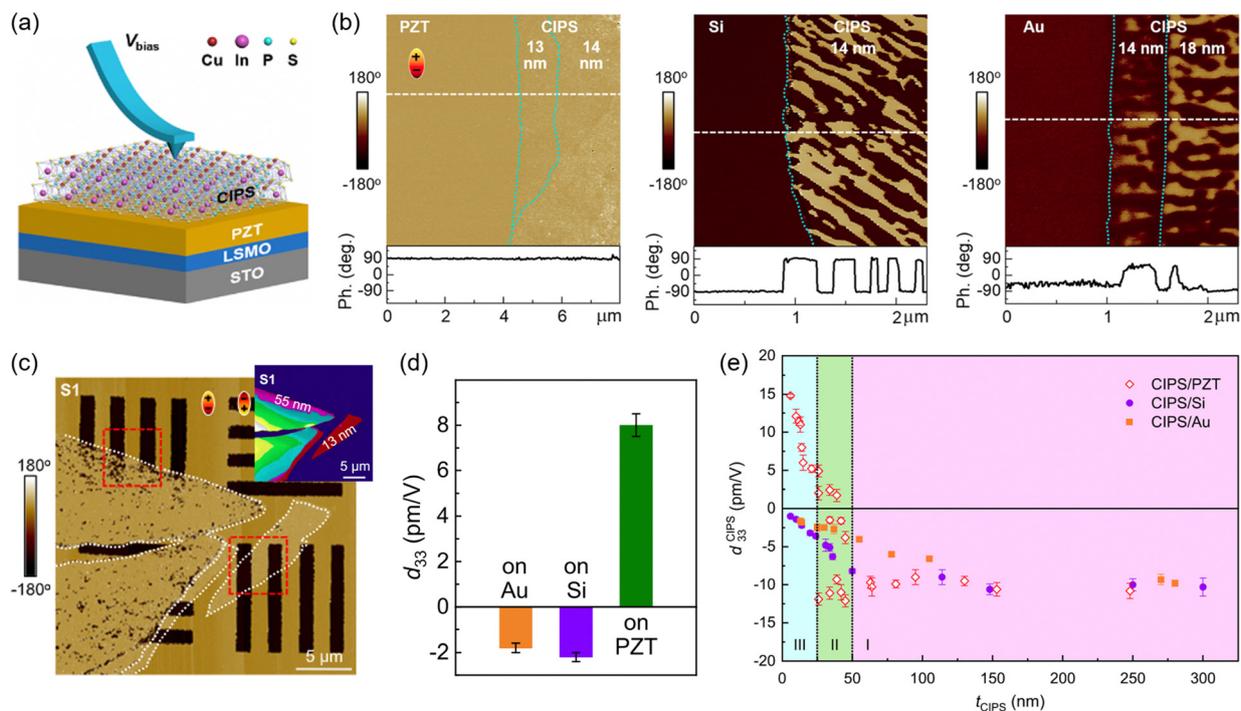
Fig. 24 Enhanced polar alignment in thin CIPS on PZT. (a) Sample schematic. (b) PFM phase images of 13–14 nm CIPS flakes transferred on PZT, Si, and Au base layers. (c) PFM phase and (inset) AFM topography images of CIPS flakes with various thickness transferred on a prepatterned domain structure on PZT. (d) Averaged d_{33} for 14 nm CIPS on Au, Si, and PZT. (e) d_{33}^{CIPS} of CIPS on PZT as a function of flake thickness. Adapted from ref. 22 with permission from American Chemical Society, copyright 2023.

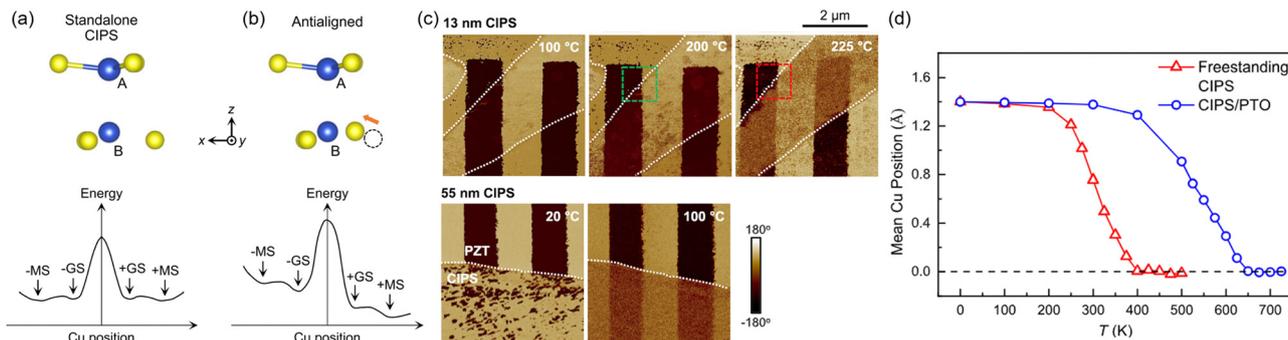**Fig. 25** Interface tuning of ferroelectricity in CIPS *via* PZT. (a) and (b) Schematics of sulfur and copper ion arrangements (upper panels) and ferroelectric quadruple–well energy profiles (lower panels) for standalone CIPS (a) and CIPS on PbTiO$_3$ with polarization antialigned (b). (c) *In situ* PFM images at selected temperatures taken on 13 nm and 55 nm CIPS on PZT, corresponding to the red boxed areas in Fig. 24(c). (d) Monte Carlo simulations of the mean Cu position at different temperatures. Reproduced from ref. 22 with permission from American Chemical Society, copyright 2023.

The enhanced polar alignment and d_{33}^{CIPS} in ultrathin CIPS flakes point to the interfacial coupling with the PZT underneath. The sign change of d_{33}^{CIPS} further suggests that the sample is settled at the metastable state (MS) rather than the ground state (GS) of the quadruple energy well (Fig. 25(a) and (b)).[178] DFT calculations of the CIPS/PbTiO$_3$ heterointerface reveal a strain-induced lattice distortion in the interfacial CIPS layer, which results in a tilted free-energy profile that favors the anti-alignment between the polarization of CIPS and PbTiO$_3$ and settles at the metastable state (Fig. 25(b)).

The titled free energy well further enhances the ferroelectric ordering energy. Fig. 25(c) shows the *in situ* PFM images of CIPS on PZT at elevated temperatures. For the 55 nm flakes, the domain structure becomes blurred at 100 °C, suggesting that it is above T_C, which is consistent with the bulk value ($T_C \sim$ 42 °C).[179] For the 13 nm CIPS, T_C is substantially enhanced to above 200 °C. Monte Carlo simulations based on atomic positions of CIPS strained on PbTiO$_3$ predict a 63% increase of T_C compared with that of standalone CIPS (Fig. 25(d)), which is in excellent agreement with the experimental results.[22] The enhanced polarization and T_C for thin CIPS on PZT, as well as their anti-aligned polarization, have been confirmed *via in situ*, temperature-dependent PL studies, which reveal an interface-strain induced lattice change in CIPS.[183] A similar enhancement of polar domain formation and the piezoelectric coefficient has been observed in the organolead trihalide perovskite CH$_3$NH$_3$PbI$_3$ interfaced with PZT,[21] which has been attributed to the over-screened ferroelectric polarization induced dipole field that promotes the polar alignment in a polar liquid state of the hybrid perovskite.[184]

6. Conclusions and perspectives

In this feature article, we use ferroelectric perovskite oxide-based heterostructures as model systems to illustrate various emergent phenomena mediated by interfacial coupling of charge, lattice, and polar symmetry. The discussion centers on epitaxial complex oxide heterostructures and ferroelectric thin films and membranes interfaced with 2D van der Waals materials. The electrostatic and mechanical boundary conditions have

profound impacts on the polar properties of ferroelectric oxide thin films, leading to large variations in the ferroelectric Curie temperature and coercive field. The T_C of epitaxial ferroelectric films can be over 300 °C higher than the bulk value due to compressive strain. It is interesting to note that the strain level can be sustained in suspended oxide membranes after being transferred on a different base layer, and the properties of the base layer (*e.g.*, surface roughness and bonding type) can affect the level of strain relaxation. The DW roughness and its thermal evolution have been systematically analyzed, which reveal the critical role of the base layer and the complex interplay of interfacial screening capacity, atomic bonding, surface morphology, and defect migration in determining the static distribution and dynamic response of the DW. The effect of the depolarization field is manifested in the ferroelectric–dielectric transition, transient negative capacitance mode, and domain formation in ferroelectric/dielectric heterostructures. The gained information is critical for understanding the polarization switching dynamics, domain size limit, and thermal stability and can facilitate the development of domain/DW-based memory and logic devices with high density, high speed, low power, and high operation temperature.

We also survey the coupling mechanisms and emergent functionalities of ferroelectric oxide-based heterointerfaces, including the ferroelectric field effect control of the electronic and magnetic states in correlated oxides and quantum transport in graphene, as well as the filtering effect of nonlinear optical response of MoS$_2$ *via* ferroelectric polarization and DWs. Nanoscale domain patterning further allows the design of 1D graphene superlattices and programmable second harmonic generation in ferroelectric/MoS$_2$ heterostructures. The interfacial strain coupling with ferroelectric thin films have been leveraged to enhance the polar alignment, piezoelectric response, and T_C in ultrathin 2D ferroelectric CIPS flakes. Various emerging device concepts have been discussed, including Mott FeFETs, ferroelectric tunnel junctions, steep slope NC FETs, electron lensing devices, and *in operando* nonlinear optical filters, highlighting their application potential in high performance, reconfigurable nanoelectronics, optoelectronics, and nano-photonics.

Our discussions showcase the rich functionalities and high application potential of ferroelectric perovskite oxide-based

heterostructures. Looking forward, we outline several potential research directions that can broaden the research portfolio based on functional design of ferroelectric oxide heterostructures.

Novel materials synthesis

For technological applications of ferroelectric oxide-gated 2D vdW FETs, it is essential to develop a scalable synthesis method and CMOS-compatible device architectures. In previous studies of 2D FeFETs, ferroelectric oxides are mainly adopted as a global back-gate.[4] Converting to a top-gate device structure involves dry-transfer of ferroelectric membranes,[28] which requires multiple fabrication steps and is not scalable. The recently developed remote epitaxy technique builds on MBE and laser MBE growth of complex oxide thin films (*e.g.*, $SrTiO_3$[185] and $BaTiO_3$[186]) on substrates buffered with porous graphene, which can be extended to other vdW buffer materials for achieving multifunctional ferroelectric heterointerfaces.

Oxide moiré engineering[29,187] based on stacking and twisting oxide membranes has attracted enormous research interest as it provides a new material platform for exploring functionalities not expected in the single-phase nano-materials, as demonstrated in the van der Waals moiré systems.[188] Unlike the van der Waals materials, which are layered by nature, the transition metal oxides are based on semi-ionic/semi-covalent bonds. This attribute both imposes challenges in materials processing, *e.g.*, for stabilizing small twisting angle phases that are thermodynamically highly unstable, and offers new opportunities capitalizing on the stronger interface interaction and potential modulation for band reconstruction. Experimentally, novel 2D polar vortex patterns have been observed in twisted $BaTiO_3$.[29] It is further conceivable to design novel polar states and magnetism in twisted oxides that are neither polar nor magnetic. The appearance of vortex–antivortex polarization and doping-induced unconventional d^0 magnetism has been theoretically predicted in twisted $SrTiO_3$ bilayers,[189] making it promising for realizing a multiferroic state that is controllable *via* the electric field effect.

Incorporation of binary ferroelectric oxides

Binary ferroelectric oxides such as doped HfO_2 and ZrO_2 are compatible with the mainstream CMOS processing and have high potential for industrial applications.[190] Single crystalline doped HfO_2 has been recently demonstrated,[191] and it offers the opportunity to investigate ferroelectricity from a new material perspective. Specifically, this class of ferroelectrics exhibit high sensitivity to surface chemistry,[192,193] possess scale-free DWs,[194] and are potentially immune to the depolarization effect.[195] It is of both fundamental and technological interest to construct HfO_2-based heterostructures and understand how the interfacial electrode would affect the ferroelectric order parameter, polarization switching dynamics, and DW configurations.

Theory-driven material discovery and functionality design

The rapid development of DFT-based computational material search, especially enabled by machine-learning, offers unforeseeable

research opportunities to design novel ferroelectric oxides and heterostructures with tailored functionalities. One direction of interest is to design ferroelectric oxide with non-trivial topology properties. It has been theoretically shown that noncentrosymmetric $BiInO_3$ is ferroelectric and can host persistent spin texture, a momentum-independent spin configuration that can be coupled with the ferroelectric polarization,[196] while the polar phase $BiInO_3$ remains to be realized experimentally.[197,198] Also of interest is to impose polar symmetry and modulate the electronic and magnetic states in perovskites by designing the oxygen octahedral rotation through epitaxial strain and superlattice engineering.[199,200] This approach has been adopted to stabilize a $BiFeO_3$-like structure[201] and anchor room temperature ferroelectricity in $CaTiO_3$.[34]

Data availability

There are no new data generated in this work.

Conflicts of interest

The authors have no conflicts to disclose.

Acknowledgements

References

1 M. Dawber, K. M. Rabe and J. F. Scott, Physics of thin-film ferroelectric oxides, *Rev. Mod. Phys.*, 2005, **77**, 1083–1130.
2 N. Setter, D. Damjanovic, L. Eng, G. Fox, S. Gevorgian, S. Hong, A. Kingon, H. Kohlstedt, N. Y. Park, G. B. Stephenson, I. Stolitchnov, A. K. Tagantsev, D. V. Taylor, T. Yamada and S. Streiffer, Ferroelectric thin films: Review of materials, properties, and applications, *J. Appl. Phys.*, 2006, **100**, 051606.
3 L. W. Martin and A. M. Rappe, Thin-film ferroelectric materials and their applications, *Nat. Rev. Mater.*, 2017, **2**, 16087.
4 X. Hong, Emerging ferroelectric transistors with nanoscale channel materials: the possibilities, the limitations, *J. Phys.: Condens. Matter*, 2016, **28**, 103003.
5 M. Bibes, J. Villegas and A. Barthelemy, Ultrathin oxide films and interfaces for electronics and spintronics, *Adv. Phys.*, 2011, **60**, 5–84.
6 S. Oh, H. Hwang and I. K. Yoo, Ferroelectric materials for neuromorphic computing, *APL Mater.*, 2019, **7**, 091109.
7 M. A. Alam, M. W. Si and P. D. D. Ye, A critical review of recent progress on negative capacitance field-effect transistors, *Appl. Phys. Lett.*, 2019, **114**, 090401.
8 N. Sezer and M. Koç, A comprehensive review on the state-of-the-art of piezoelectric energy harvesting, *Nano Energy*, 2021, **80**, 105567.
9 Y. Zhang, W. Jie, P. Chen, W. Liu and J. Hao, Ferroelectric and Piezoelectric Effects on the Optical Process in Advanced Materials and Devices, *Adv. Mater.*, 2018, **30**, 1707007.
10 C. H. Ahn, J. M. Triscone and J. Mannhart, Electric field effect in correlated oxide systems, *Nature*, 2003, **424**, 1015–1018.

11 C. H. Ahn, A. Bhattacharya, M. Di Ventra, J. N. Eckstein, C. D. Frisbie, M. E. Gershenson, A. M. Goldman, I. H. Inoue, J. Mannhart, A. J. Millis, A. F. Morpurgo, D. Natelson and J. M. Triscone, Electrostatic modification of novel materials, *Rev. Mod. Phys.*, 2006, **78**, 1185–1212.

12 C. A. F. Vaz, J. Hoffman, C. H. Ahn and R. Ramesh, Magnetoelectric Coupling Effects in Multiferroic Complex Oxide Composite Structures, *Adv. Mater.*, 2010, **22**, 2900–2918.

13 C. A. F. Vaz, Y. J. Shin, M. Bibes, K. M. Rabe, F. J. Walker and C. H. Ahn, Epitaxial ferroelectric interfacial devices, *Appl. Phys. Rev.*, 2021, **8**, 041308.

14 H. Ryu, K. Xu, D. Li, X. Hong and W. Zhu, Empowering 2D nanoelectronics *via* ferroelectricity, *Appl. Phys. Lett.*, 2020, **117**, 080503.

15 X. Hong, A. Posadas, A. Lin and C. H. Ahn, Ferroelectric-field-induced tuning of magnetism in the colossal magnetoresistive oxide La$_{1-x}$Sr$_x$MnO$_3$, *Phys. Rev. B: Condens. Matter Mater. Phys.*, 2003, **68**, 134415.

16 X. Hong, A. Posadas and C. H. Ahn, Examining the screening limit of field effect devices *via* the metal–insulator transition, *Appl. Phys. Lett.*, 2005, **86**, 142501.

17 A. K. Yadav, C. T. Nelson, S. L. Hsu, Z. Hong, J. D. Clarkson, C. M. Schlepuetz, A. R. Damodaran, P. Shafer, E. Arenholz, L. R. Dedon, D. Chen, A. Vishwanath, A. M. Minor, L. Q. Chen, J. F. Scott, L. W. Martin and R. Ramesh, Observation of polar vortices in oxide superlattices, *Nature*, 2016, **530**, 198.

18 Z. Hong, A. R. Damodaran, F. Xue, S.-L. Hsu, J. Britson, A. K. Yadav, C. T. Nelson, J.-J. Wang, J. F. Scott, L. W. Martin, R. Ramesh and L.-Q. Chen, Stability of Polar Vortex Lattice in Ferroelectric Superlattices, *Nano Lett.*, 2017, **17**, 2246–2252.

19 P. Zubko, J. C. Wojdel, M. Hadjimichael, S. Fernandez-Pena, A. Sene, I. Luk'yanchuk, J. M. Triscone and J. Iniguez, Negative capacitance in multidomain ferroelectric superlattices, *Nature*, 2016, **534**, 524.

20 A. K. Yadav, K. X. Nguyen, Z. J. Hong, P. Garcia-Fernandez, P. Aguado-Puente, C. T. Nelson, S. Das, B. Prasad, D. Kwon, S. Cheema, A. I. Khan, C. M. Hu, J. Iniguez, J. Junquera, L. Q. Chen, D. A. Muller, R. Ramesh and S. Salahuddin, Spatially resolved steady-state negative capacitance, *Nature*, 2019, **565**, 468.

21 J. Song, Z. Xiao, B. Chen, S. Prockish, X. Chen, A. Rajapitamahuni, L. Zhang, J. Huang and X. Hong, Enhanced Piezoelectric Response in Hybrid Lead Halide Perovskite Thin Films *via* Interfacing with Ferroelectric PbZr$_{0.2}$Ti$_{0.8}$O$_3$, *ACS Appl. Mater. Interfaces*, 2018, **10**, 19218–19225.

22 K. Wang, D. Li, J. Wang, Y. Hao, H. Anderson, L. Yang and X. Hong, Interface-Tuning of Ferroelectricity and Quadruple-Well State in CuInP$_2$S$_6$ *via* Ferroelectric Oxide, *ACS Nano*, 2023, **17**, 15787–15795.

23 T. Li, H. Chen, K. Wang, Y. Hao, L. Zhang, K. Watanabe, T. Taniguchi and X. Hong, Transport Anisotropy in One-Dimensional Graphene Superlattice in the High Kronig-Penney Potential Limit, *Phys. Rev. Lett.*, 2024, **132**, 056204.

24 D. Li, X. Huang, Z. Xiao, H. Chen, L. Zhang, Y. Hao, J. Song, D.-F. Shao, E. Y. Tsymbal, Y. Lu and X. Hong, Polar coupling enabled nonlinear optical filtering at MoS$_2$/ferroelectric heterointerfaces, *Nat. Commun.*, 2020, **11**, 1422.

25 D. Li, X. Huang, Q. Wu, L. Zhang, Y. Lu and X. Hong, Ferroelectric Domain Control of Nonlinear Light Polarization in MoS$_2$ *via* PbZr$_{0.2}$Ti$_{0.8}$O$_3$ Thin Films and Free-Standing Membranes, *Adv. Mater.*, 2023, **35**, 2208825.

26 S. R. Bakaul, J. Kim, S. Hong, M. J. Cherukara, T. Zhou, L. Stan, C. R. Serrao, S. Salahuddin, A. K. Petford-Long, D. D. Fong and M. V. Holt, Ferroelectric Domain Wall Motion in Freestanding Single-Crystal Complex Oxide Thin Film, *Adv. Mater.*, 2020, **32**, 1907036.

27 S. R. Bakaul, S. Prokhorenko, Q. Zhang, Y. Nahas, Y. S. Hu, A. Petford-Long, L. Bellaiche and N. Valanoor, Freestanding Ferroelectric Bubble Domains, *Adv. Mater.*, 2021, **33**, 2105432.

28 Q. Wu, K. Wang, A. Simpson, Y. Hao, J. Wang, D. Li and X. Hong, Electrode Effect on Ferroelectricity in Free-Standing Membranes of PbZr$_{0.2}$Ti$_{0.8}$O$_3$, *ACS Nanosci. Au*, 2023, **3**, 482–490.

29 G. Sánchez-Santolino, V. Rouco, S. Puebla, H. Aramberri, V. Zamora, M. Cabero, F. A. Cuellar, C. Munuera, F. Mompean, M. Garcia-Hernandez, A. Castellanos-Gomez, J. Iñiguez, C. Leon and J. Santamaria, A 2D ferroelectric vortex pattern in twisted BaTiO$_3$ freestanding layers, *Nature*, 2024, **626**, 529.

30 A. Lin, X. Hong, V. Wood, A. A. Verevkin, C. H. Ahn, R. A. McKee, F. J. Walker and E. D. Specht, Epitaxial growth of Pb(Zr$_{0.2}$Ti$_{0.8}$)O$_3$ on Si and its nanoscale piezoelectric properties, *Appl. Phys. Lett.*, 2001, **78**, 2034–2036.

31 C. Dubourdieu, J. Bruley, T. M. Arruda, A. Posadas, J. Jordan-Sweet, M. M. Frank, E. Cartier, D. J. Frank, S. V. Kalinin, A. A. Demkov and V. Narayanan, Switching of ferroelectric polarization in epitaxial BaTiO$_3$ films on silicon without a conducting bottom electrode, *Nat. Nanotechnol.*, 2013, **8**, 748–754.

32 R. M. Moghadam, Z. Xiao, K. Ahmadi-Majlan, E. D. Grimley, M. Bowden, P.-V. Ong, S. A. Chambers, J. M. Lebeau, X. Hong, P. V. Sushko and J. H. Ngai, An Ultrathin Single Crystalline Relaxor Ferroelectric Integrated on a High Mobility Semiconductor, *Nano Lett.*, 2017, **17**, 6248–6257.

33 A. R. Damodaran, J. C. Agar, S. Pandya, Z. H. Chen, L. Dedon, R. J. Xu, B. Apgar, S. Saremi and L. W. Martin, New modalities of strain-control of ferroelectric thin films, *J. Phys.: Condens. Matter*, 2016, **28**, 263001.

34 J. R. Kim, J. Jang, K.-J. Go, S. Y. Park, C. J. Roh, J. Bonini, J. Kim, H. G. Lee, K. M. Rabe, J. S. Lee, S.-Y. Choi, T. W. Noh and D. Lee, Stabilizing hidden room-temperature ferroelectricity *via* a metastable atomic distortion pattern, *Nat. Commun.*, 2020, **11**, 4944.

35 S. A. Chambers, Epitaxial growth and properties of doped transition metal and complex oxide films, *Adv. Mater.*, 2010, **22**, 219–248.

36 K. R. Talley, C. L. Perkins, D. R. Diercks, G. L. Brennecka and A. Zakutayev, Synthesis of LaWN$_3$ nitride perovskite with polar symmetry, *Science*, 2021, **374**, 1488–1491.

37 X. Hong, Nitride perovskite becomes polar, *Science*, 2021, **374**, 1445–1446.

38 J. P. Podkaminer, J. J. Patzner, B. A. Davidson and C. B. Eom, Real-time and *in situ* monitoring of sputter deposition with RHEED for atomic layer controlled growth, *APL Mater.*, 2016, **4**, 086111.

39 Y. Hao, T. Li, Y. Yun, X. Li, X. Chen, J. Song, Z. Ahmadi, J. E. Shield, X. Xu and X. Hong, Tuning Negative Capacitance in PbZr$_{0.2}$Ti$_{0.8}$O$_3$/SrTiO$_3$ Heterostructures *via* Layer Thickness Ratio, *Phys. Rev. Appl.*, 2021, **16**, 034004.

40 X. Chen, X. Zhang, M. A. Koten, H. Chen, Z. Xiao, L. Zhang, J. E. Shield, P. A. Dowben and X. Hong, Interfacial Charge Engineering in Ferroelectric-Controlled Mott Transistors, *Adv. Mater.*, 2017, **29**, 1701385.

41 Y. Hao, X. Chen, L. Zhang, M.-G. Han, W. Wang, Y.-W. Fang, H. Chen, Y. Zhu and X. Hong, Record high room temperature resistance switching in ferroelectric-gated Mott transistors unlocked by interfacial charge engineering, *Nat. Commun.*, 2023, **14**, 8247.

42 D. Lu, D. J. Baek, S. S. Hong, L. F. Kourkoutis, Y. Hikita and H. Y. Hwang, Synthesis of freestanding single-crystal perovskite films and heterostructures by etching of sacrificial water-soluble layers, *Nat. Mater.*, 2016, **15**, 1255–1260.

43 D. Pesquera, A. Fernandez, E. Khestanova and L. W. Martin, Freestanding complex-oxide membranes, *J. Phys.: Condens. Matter*, 2022, **34**, 383001.

44 S. Puebla, T. Pucher, V. Rouco, G. Sanchez-Santolino, Y. Xie, V. Zamora, F. A. Cuellar, F. J. Mompean, C. Leon, J. O. Island, M. Garcia-Hernandez, J. Santamaria, C. Munuera and A. Castellanos-Gomez, Combining Freestanding Ferroelectric Perovskite Oxides with Two-Dimensional Semiconductors for High Performance Transistors, *Nano Lett.*, 2022, **22**, 7457–7466.

45 J. Choi, K. J. Crust, L. Z. Li, K. Lee, J. L. Luo, J. P. So, K. Watanabe, T. Taniguchi, H. Y. Hwang, K. F. Mak, J. Shan and G. D. Fuchs, Tuning Exciton Emission *via* Ferroelectric Polarization at a Heterogeneous Interface between a Monolayer Transition Metal Dichalcogenide and a Perovskite Oxide Membrane, *Nano Lett.*, 2024, **24**, 8948–8955.

46 T. Pucher, S. Puebla, V. Zamora, E. S. Viso, V. Rouco, C. Leon, M. Garcia-Hernandez, J. Santamaria, C. Munuera and A. Castellanos-Gomez, Strong Electrostatic Control of Excitonic Features in MoS$_2$ by a Free-Standing Ultrahigh-κ Ferroelectric Perovskite, *Adv. Funct. Mater.*, 2024, **34**, 2409447.

47 H. G. Wang, V. Harbola, Y. J. Wu, P. A. van Aken and J. Mannhart, Interface Design beyond Epitaxy: Oxide Heterostructures Comprising Symmetry-Forbidden Interfaces, *Adv. Mater.*, 2024, **36**, 202405065.

48 K. Wang, Y. Hao, L. Zhang, Y. Zhang, X. Chen and X. Hong, Effect of correlated oxide electrodes on disorder pinning and thermal

roughening of ferroelectric domain walls in epitaxial $PbZr_{0.2}Ti_{0.8}O_3$ thin films, *Phys. Rev. Mater.*, 2021, **5**, 074402.

49 X. Hong, A. Posadas, K. Zou, C. H. Ahn and J. Zhu, High-Mobility Few-Layer Graphene Field Effect Transistors Fabricated on Epitaxial Ferroelectric Gate Oxides, *Phys. Rev. Lett.*, 2009, **102**, 136808.

50 X. Hong, J. Hoffman, A. Posadas, K. Zou, C. H. Ahn and J. Zhu, Unusual resistance hysteresis in n-layer graphene field effect transistors fabricated on ferroelectric $Pb(Zr_{0.2}Ti_{0.8})O_3$, *Appl. Phys. Lett.*, 2010, **97**, 033114.

51 C. Baeumer, S. P. Rogers, R. J. Xu, L. W. Martin and M. Shim, Tunable Carrier Type and Density in Graphene/$PbZr_{0.2}Ti_{0.8}O_3$ Hybrid Structures through Ferroelectric Switching, *Nano Lett.*, 2013, **13**, 1693–1698.

52 A. Rajapitamahuni, J. Hoffman, C. H. Ahn and X. Hong, Examining Graphene Field Effect Sensors for Ferroelectric Thin Film Studies, *Nano Lett.*, 2013, **13**, 4374–4379.

53 M. H. Yusuf, B. Nielsen, M. Dawber and X. Du, Extrinsic and Intrinsic Charge Trapping at the Graphene/Ferroelectric Interface, *Nano Lett.*, 2014, **14**, 5437–5444.

54 A. Lipatov, P. Sharma, A. Gruverman and A. Sinitskii, Optoelectrical Molybdenum Disulfide (MoS_2)—Ferroelectric Memories, *ACS Nano*, 2015, **9**, 8089–8098.

55 J. Song, Y. Qi, Z. Xiao, K. Wang, D. Li, S.-H. Kim, A. I. Kingon, A. M. Rappe and X. Hong, Domain wall enabled steep slope switching in MoS_2 transistors towards hysteresis-free operation, *npj 2D Mater. Appl.*, 2022, **6**, 77.

56 E. B. Song, B. Lian, S. M. Kim, S. Lee, T. K. Chung, M. S. Wang, C. F. Zeng, G. Y. Xu, K. Wong, Y. Zhou, H. I. Rasool, D. H. Seo, H. J. Chung, J. Heo, S. Seo and K. L. Wang, Robust bi-stable memory operation in single-layer graphene ferroelectric memory, *Appl. Phys. Lett.*, 2011, **99**, 042109.

57 C. Baeumer, D. Saldana-Greco, J. M. P. Martirez, A. M. Rappe, M. Shim and L. W. Martin, Ferroelectrically driven spatial carrier density modulation in graphene, *Nat. Commun.*, 2015, **6**, 6136.

58 A. Nguyen, P. Sharma, T. Scott, E. Preciado, V. Klee, D. Sun, I. H. D. Lu, D. Barroso, S. Kim, V. Y. Shur, A. R. Akhmatkhanov, A. Gruverman, L. Bartels and P. A. Dowben, Toward Ferroelectric Control of Monolayer MoS_2, *Nano Lett.*, 2015, **15**, 3364–3369.

59 F. Lo Presti, A. L. Pellegrino and G. Malandrino, Metal–Organic Chemical Vapor Deposition of Oxide Perovskite Films: A Facile Route to Complex Functional Systems, *Adv. Mater. Interfaces*, 2022, **9**, 2102501.

60 S. Liu, D. Zou, X. Yu, Z. Wang and Z. Yang, Transfer-Free PZT Thin Films for Flexible Nanogenerators Derived from a Single-Step Modified Sol–Gel Process on 2D Mica, *ACS Appl. Mater. Interfaces*, 2020, **12**, 54991–54999.

61 K. S. Novoselov, A. K. Geim, S. V. Morozov, D. Jiang, Y. Zhang, S. V. Dubonos, I. V. Grigorieva and A. A. Firsov, Electric Field Effect in Atomically Thin Carbon Films, *Science*, 2004, **306**, 666–669.

62 Y. Huang, E. Sutter, N. N. Shi, J. Zheng, T. Yang, D. Englund, H.-J. Gao and P. Sutter, Reliable Exfoliation of Large-Area High-Quality Flakes of Graphene and Other Two-Dimensional Materials, *ACS Nano*, 2015, **9**, 10612–10620.

63 Y. Huang, Y.-H. Pan, R. Yang, L.-H. Bao, L. Meng, H.-L. Luo, Y.-Q. Cai, G.-D. Liu, W.-J. Zhao, Z. Zhou, L.-M. Wu, Z.-L. Zhu, M. Huang, L.-W. Liu, L. Liu, P. Cheng, K.-H. Wu, S.-B. Tian, C.-Z. Gu, Y.-G. Shi, Y.-F. Guo, Z. G. Cheng, J.-P. Hu, L. Zhao, G.-H. Yang, E. Sutter, P. Sutter, Y.-L. Wang, W. Ji, X.-J. Zhou and H.-J. Gao, Universal mechanical exfoliation of large-area 2D crystals, *Nat. Commun.*, 2020, **11**, 2453.

64 M. Velický, G. E. Donnelly, W. R. Hendren, S. McFarland, D. Scullion, W. J. I. DeBenedetti, G. C. Correa, Y. Han, A. J. Wain, M. A. Hines, D. A. Muller, K. S. Novoselov, H. D. Abruña, R. M. Bowman, E. J. G. Santos and F. Huang, Mechanism of Gold-Assisted Exfoliation of Centimeter-Sized Transition-Metal Dichalcogenide Monolayers, *ACS Nano*, 2018, **12**, 10463–10472.

65 Y. Wu, I. Abdelwahab, K. C. Kwon, I. Verzhbitskiy, L. Wang, W. H. Liew, K. Yao, G. Eda, K. P. Loh, L. Shen and S. Y. Quek, Data-driven discovery of high performance layered van der Waals piezoelectric $NbOI_2$, *Nat. Commun.*, 2022, **13**, 1884.

66 A. Castellanos-Gomez, M. Buscema, R. Molenaar, V. Singh, L. Janssen, H. S. J. van der Zant and G. A. Steele, Deterministic transfer of two-dimensional materials by all-dry viscoelastic stamping, *2D Mater.*, 2014, **1**, 011002.

67 K. Kinoshita, R. Moriya, M. Onodera, Y. Wakafuji, S. Masubuchi, K. Watanabe, T. Taniguchi and T. Machida, Dry release transfer of graphene and few-layer h-BN by utilizing thermoplasticity of polypropylene carbonate, *npj 2D Mater. Appl.*, 2019, **3**, 22.

68 F. Pizzocchero, L. Gammelgaard, B. S. Jessen, J. M. Caridad, L. Wang, J. Hone, P. Bøggild and T. J. Booth, The hot pick-up technique for batch assembly of van der Waals heterostructures, *Nat. Commun.*, 2016, **7**, 11894.

69 P. J. Zomer, M. H. D. Guimarães, J. C. Brant, N. Tombros and B. J. van Wees, Fast pick up technique for high quality heterostructures of bilayer graphene and hexagonal boron nitride, *Appl. Phys. Lett.*, 2014, **105**, 013101.

70 W. Huang, Y. Zhang, M. Song, B. Wang, H. Hou, X. Hu, X. Chen and T. Zhai, Encapsulation strategies on 2D materials for field effect transistors and photodetectors, *Chin. Chem. Lett.*, 2022, **33**, 2281–2290.

71 M. Saeed, Y. Alshammari, S. A. Majeed and E. Al-Nasrallah, Chemical Vapour Deposition of Graphene—Synthesis, Characterisation, and Applications: A Review, *Molecules*, 2020, **25**, 3856.

72 M. Wu, Y. Xiao, Y. Zeng, Y. Zhou, X. Zeng, L. Zhang and W. Liao, Synthesis of two-dimensional transition metal dichalcogenides for electronics and optoelectronics, *InfoMat*, 2021, **3**, 362–396.

73 J. Wang, J. Kang, S. Chyczewski, Y. Lin, H. Lee, W. Zhu and X. Hong, Progress and challenges in the synthesis of two-dimensional van der Waals ferroic materials and heterostructures, *J. Phys. D: Appl. Phys.*, 2025, **58**, 063001.

74 S. O. Leontsev and R. E. Eitel, Progress in engineering high strain lead-free piezoelectric ceramics, *Sci. Technol. Adv. Mater.*, 2010, **11**, 044302.

75 F. V. E. Hensling, C. Xu, F. Gunkel and R. Dittmann, Unraveling the enhanced Oxygen Vacancy Formation in Complex Oxides during Annealing and Growth, *Sci. Rep.*, 2017, **7**, 39953.

76 L. Zhang, X. G. Chen, H. J. Gardner, M. A. Koten, J. E. Shield and X. Hong, Effect of strain on ferroelectric field effect in strongly correlated oxide $Sm_{0.5}Nd_{0.5}NiO_3$, *Appl. Phys. Lett.*, 2015, **107**, 152906.

77 Y. W. So, D. J. Kim, T. W. Noh, J.-G. Yoon and T. K. Song, Polarization switching kinetics of epitaxial $Pb(Zr_{0.4}Ti_{0.6})O_3$ thin films, *Appl. Phys. Lett.*, 2005, **86**, 092905.

78 P. K. Panda and B. Sahoo, PZT to Lead Free Piezo Ceramics: A Review, *Ferroelectrics*, 2015, **474**, 128–143.

79 J. W. Reiner, A. M. Kolpak, Y. Segal, K. F. Garrity, S. Ismail-Beigi, C. H. Ahn and F. J. Walker, Crystalline Oxides on Silicon, *Adv. Mater.*, 2010, **22**, 2919–2938.

80 S. R. Bakaul, C. R. Serrao, M. Lee, C. W. Yeung, A. Sarker, S.-L. Hsu, A. K. Yadav, L. Dedon, L. You, A. I. Khan, J. D. Clarkson, C. Hu, R. Ramesh and S. Salahuddin, Single crystal functional oxides on silicon, *Nat. Commun.*, 2016, **7**, 10547.

81 M. P. Warusawithana, C. Cen, C. R. Sleasman, J. C. Woicik, Y. Li, L. F. Kourkoutis, J. A. Klug, H. Li, P. Ryan, L.-P. Wang, M. Bedzyk, D. A. Muller, L.-Q. Chen, J. Levy and D. G. Schlom, A Ferroelectric Oxide Made Directly on Silicon, *Science*, 2009, **324**, 367–370.

82 H. W. Jang, A. Kumar, S. Denev, M. D. Biegalski, P. Maksymovych, C. W. Bark, C. T. Nelson, C. M. Folkman, S. H. Baek, N. Balke, C. M. Brooks, D. A. Tenne, D. G. Schlom, L. Q. Chen, X. Q. Pan, S. V. Kalinin, V. Gopalan and C. B. Eom, Ferroelectricity in Strain-Free $SrTiO_3$ Thin Films, *Phys. Rev. Lett.*, 2010, **104**, 197601.

83 T. Emig and T. Nattermann, Disorder driven roughening transitions of elastic manifolds and periodic elastic media, *Eur. Phys. J. B*, 1999, **8**, 525–546.

84 T. Giamarchi, A. B. Kolton and A. Rosso, *Jamming, Yielding, and Irreversible Deformation in Condensed Matter*, C. Miguel and J. M. Rubi, Springer, Berlin, Heidelberg, 2006, vol. 688, pp. 91.

85 P. Paruch, T. Giamarchi and J.-M. Triscone, Domain wall roughness in epitaxial ferroelectric $PbZr_{0.2}Ti_{0.8}O_3$ thin films, *Phys. Rev. Lett.*, 2005, **94**, 197601.

86 P. Paruch, A. B. Kolton, X. Hong, C. H. Ahn and T. Giamarchi, Thermal quench effects on ferroelectric domain walls, *Phys. Rev. B: Condens. Matter Mater. Phys.*, 2012, **85**, 214115.

87 A. B. Kolton, A. Rosso and T. Giamarchi, Creep Motion of an Elastic String in a Random Potential, *Phys. Rev. Lett.*, 2005, **94**, 047002.

88 J. Guyonnet, E. Agoritsas, S. Bustingorry, T. Giamarchi and P. Paruch, Multiscaling analysis of ferroelectric domain wall roughness, *Phys. Rev. Lett.*, 2012, **109**, 147601.

89 E. Agoritsas, V. Lecomte and T. Giamarchi, Temperature-induced crossovers in the static roughness of a one-dimensional interface, *Phys. Rev. B: Condens. Matter Mater. Phys.*, 2010, **82**, 184207.

90 E. Agoritsas, V. Lecomte and T. Giamarchi, Disordered elastic systems and one-dimensional interfaces, *Phys. Rev. B: Condens. Matter Mater. Phys.*, 2012, **407**, 1725–1733.

91 S. Catalano, M. Gibert, J. Fowlie, J. Íñiguez, J. M. Triscone and J. Kreisel, Rare-earth nickelates $RNiO_3$: thin films and heterostructures, *Rep. Prog. Phys.*, 2018, **81**, 046501.

92 X. Hong, J. B. Yau, J. D. Hoffman, C. H. Ahn, Y. Bason and L. Klein, Effect of electric field doping on the anisotropic magnetoresistance in doped manganites, *Phys. Rev. B: Condens. Matter Mater. Phys.*, 2006, **74**, 174406.

93 A. G. Zaitsev, A. Beck, A. K. Jaiswal, R. Singh, R. Schneider, M. Le Tacon and D. Fuchs, Anomalous pressure dependence of the electronic transport and anisotropy in $SrIrO_3$ films, *J. Phys.: Condens. Matter*, 2020, **32**, 345601.

94 G. A. Rossetti, Structure and bonding in $PbZrO_3$–$PbTiO_3$ (PZT) alloys, *Br. Ceram. Trans.*, 2004, **103**, 83–87.

95 M. V. Raymond and D. M. Smyth, Defects and charge transport in perovskite ferroelectrics, *J. Phys. Chem. Solids*, 1996, **57**, 1507–1511.

96 N. Lee, Y. Lansac, H. Hwang and Y. H. Jang, Switching mechanism of $Al/La_{1-x}Sr_xMnO_3$ resistance random access memory. I. Oxygen vacancy formation in perovskites, *RSC Adv.*, 2015, **5**, 102772.

97 A. Malashevich and S. Ismail-Beigi, First-principles study of oxygen-deficient $LaNiO_3$ structures, *Phys. Rev. B: Condens. Matter Mater. Phys.*, 2015, **92**, 144102.

98 G. Wan, J. W. Freeland, J. Kloppenburg, G. Petretto, J. N. Nelson, D.-Y. Kuo, C.-J. Sun, J. Wen, J. T. Diulus, G. S. Herman, Y. Dong, R. Kou, J. Sun, S. Chen, K. M. Shen, D. G. Schlom, G.-M. Rignanese, G. Hautier, D. D. Fong, Z. Feng, H. Zhou and J. Suntivich, Amorphization mechanism of $SrIrO_3$ electrocatalyst: How oxygen redox initiates ionic diffusion and structural reorganization, *Sci. Adv.*, 2021, 7, eabc7323.

99 Y. Zhang, Y. Hao, L. Zhang, K. Wang and X. Hong, High electroresistance in all-oxide ferroelectric tunnel junctions enabled by a narrow bandgap Mott insulator electrode, *Appl. Phys. Lett.*, 2024, **125**, 102904.

100 A. Rajapitamahuni, L. L. Tao, Y. Hao, J. Song, X. Xu, E. Y. Tsymbal and X. Hong, Ferroelectric polarization control of magnetic anisotropy in $PbZr_{0.2}Ti_{0.8}O_3/La_{0.8}Sr_{0.2}MnO_3$ heterostructures, *Phys. Rev. Mater.*, 2019, **3**, 021401.

101 A. Urushibara, Y. Moritomo, T. Arima, A. Asamitsu, G. Kido and Y. Tokura, Insulator-metal transition and giant magnetoresistance in $La_{1-x}Sr_xMnO_3$, *Phys. Rev. B: Condens. Matter Mater. Phys.*, 1995, **51**, 14103–14109.

102 R. Scherwitzl, S. Gariglio, M. Gabay, P. Zubko, M. Gibert and J. M. Triscone, Metal-Insulator Transition in Ultrathin $LaNiO_3$ Films, *Phys. Rev. Lett.*, 2011, **106**, 246403.

103 L. Zhang, H. Gardner, X. Chen, V. Singh and X. Hong, Strain induced modulation of the correlated transport in epitaxial $Sm_{0.5}Nd_{0.5}NiO_3$ thin films, *J. Phys.: Condens. Matter*, 2015, **27**, 132201.

104 G. Catalan, Progress in perovskite nickelate research, *Phase Transitions*, 2008, **81**, 729–749.

105 R. Scherwitzl, P. Zubko, I. G. Lezama, S. Ono, A. F. Morpurgo, G. Catalan and J. M. Triscone, Electric-Field Control of the Metal-Insulator Transition in Ultrathin $NdNiO_3$ Films, *Adv. Mater.*, 2010, **22**, 5517–5520.

106 A. Malashevich, M. S. J. Marshall, C. Visani, A. S. Disa, H. Xu, F. J. Walker, C. H. Ahn and S. Ismail-Beigi, Controlling Mobility in Perovskite Oxides by Ferroelectric Modulation of Atomic-Scale Interface Structure, *Nano Lett.*, 2018, **18**, 573–578.

107 M. Golalikhani, Q. Lei, R. U. Chandrasena, L. Kasaei, H. Park, J. Bai, P. Orgiani, J. Ciston, G. E. Sterbinsky, D. A. Arena, P. Shafer, E. Arenholz, B. A. Davidson, A. J. Millis, A. X. Gray and X. X. Xi, Nature of the metal-insulator transition in few-unit-cell-thick $LaNiO_3$ films, *Nat. Commun.*, 2018, **9**, 2206.

108 C. Zhou, D. M. Newns, J. A. Misewich and P. C. Pattnaik, A field effect transistor based on the Mott transition in a molecular layer, *Appl. Phys. Lett.*, 1997, **70**, 598–600.

109 S. Hormoz and S. Ramanathan, Limits on vanadium oxide Mott metal-insulator transition field-effect transistors, *Solid-State Electron.*, 2010, **54**, 654–659.

110 Y. Watanabe, Epitaxial All-Perovskite Ferroelectric Field-Effect Transistor with a Memory Retention, *Appl. Phys. Lett.*, 1995, **66**, 1770–1772.

111 C. H. Ahn, S. Gariglio, P. Paruch, T. Tybell, L. Antognazza and J. M. Triscone, Electrostatic modulation of superconductivity in ultrathin $GdBa_2Cu_3O_{7-x}$ films, *Science*, 1999, **284**, 1152–1155.

112 S. Gariglio, C. H. Ahn, D. Matthey and J. M. Triscone, Electrostatic Tuning of the Hole Density in $NdBa_2Cu_3O_{7-delta}$ Films and its Effect on the Hall Response, *Phys. Rev. Lett.*, 2002, **88**, 067002.

113 J. Hoffman, X. Hong and C. H. Ahn, Device performance of ferroelectric/correlated oxide heterostructures for non-volatile memory applications, *Nanotechnology*, 2011, **22**, 254014.

114 H. Yamada, M. Marinova, P. Altuntas, A. Crassous, L. Begon-Lours, S. Fusil, E. Jacquet, V. Garcia, K. Bouzehouane, A. Gloter, J. E. Villegas, A. Barthelemy and M. Bibes, Ferroelectric control of a Mott insulator, *Sci. Rep.*, 2013, **3**, 2834.

115 C. H. Ahn, T. Tybell, L. Antognazza, K. Char, R. H. Hammond, M. R. Beasley, Ø. Fischer and J.-M. Triscone, Local, Nonvolatile Electronic Writing of Epitaxial $Pb(Zr_{0.52}Ti_{0.48})O_3/SrRuO_3$ Heterostructures, *Science*, 1997, **276**, 1100–1103.

116 K. Zhang, X. Jia, K. Cao, J. Wang, Y. Zhang, K. Lin, L. Chen, X. Feng, Z. Zheng, Z. Zhang, Y. Zhang and W. Zhao, High On/Off Ratio Spintronic Multi-Level Memory Unit for Deep Neural Network, *Adv. Sci.*, 2022, **9**, 2103357.

117 X. J. Lou, Polarization fatigue in ferroelectric thin films and related materials, *J. Appl. Phys.*, 2009, **105**, 024101.

118 S. Chu, Y. Hao, S. Feng, X. Hong and K. Lai, Room-temperature modulation of microwave conductivity in ferroelectric-gated correlated oxides, *Appl. Phys. Lett.*, 2024, **125**, 182902.

119 X. Hong, F. Xiao, J. W. Reiner, A. Posadas and C. H. Ahn, Growth and characterization of $La_{0.8}Sr_{0.2}MnO_3/Pb(Zr_{0.2}Ti_{0.8})O_3/La_{0.8}Sr_{0.2}MnO_3$ heterostructures for three-dimensional circuit studies, *Ann. Phys.*, 2004, **516**, 15–19.

120 V. Garcia and M. Bibes, Ferroelectric tunnel junctions for information storage and processing, *Nat. Commun.*, 2014, **5**, 4289.

121 E. Y. Tsymbal and H. Kohlstedt, Tunneling Across a Ferroelectric, *Science*, 2006, **313**, 181–183.

122 M. Y. Zhuravlev, R. F. Sabirianov, S. S. Jaswal and E. Y. Tsymbal, Giant Electroresistance in Ferroelectric Tunnel Junctions, *Phys. Rev. Lett.*, 2005, **94**, 246802.

123 Y. Yin and Q. Li, A review on all-perovskite multiferroic tunnel junctions, *J. Materiomics*, 2017, **3**, 245–254.

124 L. Chen, J. Zhou, X. Zhang, K. Ding, J. Ding, Z. Sun and X. Wang, Low-Temperature Tunneling Electroresistance in Ferromagnetic Metal/Ferroelectric/Semiconductor Tunnel Junctions, *ACS Appl. Mater. Interfaces*, 2021, **13**, 23282–23288.

125 J. Ruan, X. Qiu, Z. Yuan, D. Ji, P. Wang, A. Li and D. Wu, Improved memory functions in multiferroic tunnel junctions with a dielectric/ferroelectric composite barrier, *Appl. Phys. Lett.*, 2015, **107**, 232902.

126 Y. W. Yin, M. Raju, W. J. Hu, X. J. Weng, X. G. Li and Q. Li, Coexistence of tunneling magnetoresistance and electroresistance at room temperature in $La_{0.7}Sr_{0.3}MnO_3/(Ba, Sr)TiO_3/La_{0.7}Sr_{0.3}MnO_3$ multiferroic tunnel junctions, *J. Appl. Phys.*, 2011, **109**, 07D915.

127 Y. W. Yin, J. D. Burton, Y. M. Kim, A. Y. Borisevich, S. J. Pennycook, S. M. Yang, T. W. Noh, A. Gruverman, X. G. Li, E. Y. Tsymbal and Q. Li, Enhanced tunnelling electroresistance effect due to a ferroelectrically induced phase transition at a magnetic complex oxide interface, *Nat. Mater.*, 2013, **12**, 397–402.

128 Q. H. Qin, L. Äkäslompolo, N. Tuomisto, L. Yao, S. Majumdar, J. Vijayakumar, A. Casiraghi, S. Inkinen, B. Chen, A. Zugarramurdi, M. Puska and S. van Dijken, Resistive Switching in All-Oxide Ferroelectric Tunnel Junctions with Ionic Interfaces, *Adv. Mater.*, 2016, **28**, 6852–6859.

129 H. J. Park, C. H. Sohn, D. W. Jeong, G. Cao, K. W. Kim, S. J. Moon, H. Jin, D.-Y. Cho and T. W. Noh, Phonon-assisted optical excitation in the narrow bandgap Mott insulator $Sr_3Ir_2O_7$, *Phys. Rev. B: Condens. Matter Mater. Phys.*, 2014, **89**, 155115.

130 D. Preziosi, I. Fina, E. Pippel, D. Hesse, X. Marti, F. Bern, M. Ziese and M. Alexe, Tailoring the interfacial magnetic anisotropy in multiferroic field-effect devices, *Phys. Rev. B: Condens. Matter Mater. Phys.*, 2014, **90**, 125155.

131 D. Preziosi, M. Alexe, D. Hesse and M. Salluzzo, Electric-field control of the orbital occupancy and magnetic moment of a transition-metal oxide, *Phys. Rev. Lett.*, 2015, **115**, 157401.

132 H. J. A. Molegraaf, J. Hoffman, C. A. F. Vaz, S. Gariglio, D. van der Marel, C. H. Ahn and J. M. Triscone, Magnetoelectric Effects in Complex Oxides with Competing Ground States, *Adv. Mater.*, 2009, **21**, 3470.

133 C. A. F. Vaz, J. Hoffman, Y. Segal, J. W. Reiner, R. D. Grober, Z. Zhang, C. H. Ahn and F. J. Walker, Origin of the Magnetoelectric Coupling Effect in $Pb(Zr_{0.2}Ti_{0.8}O_3/La_{0.8}Sr_{0.2}MnO_3)$ Multiferroic Heterostructures, *Phys. Rev. Lett.*, 2010, **104**, 127202.

134 I. Zutic, J. Fabian and S. D. Sarma, Spintronics: Fundamentals and applications, *Rev. Mod. Phys.*, 2004, **76**, 323.

135 T. Li, L. Zhang and X. Hong, Anisotropic magnetoresistance and planar Hall effect in correlated and topological materials, *J. Vac. Sci. Technol., A*, 2021, **40**, 010807.

136 L. Zhang, A. Rajapitamahuni, Y. Hao and X. Hong, Probing magnetic anisotropy in epitaxial $La_{0.67}Sr_{0.33}MnO_3$ thin films and nanostructures *via* planar Hall effect, *Proc. SPIE*, 2018, **10732**, 107320F.

137 A. Rajapitamahuni, L. Zhang, M. A. Koten, V. R. Singh, J. D. Burton, E. Y. Tsymbal, J. E. Shield and X. Hong, Giant Enhancement of Magnetic Anisotropy in Ultrathin Manganite Films *via* Nanoscale 1D Periodic Depth Modulation, *Phys. Rev. Lett.*, 2016, **116**, 187201.

138 H. W. Park, J. Roh, Y. B. Lee and C. S. Hwang, Modeling of Negative Capacitance in Ferroelectric Thin Films, *Adv. Mater.*, 2019, **31**, 1805266.

139 T. Li, *Emergent Phenomena in Ferroelectric-Dielectric and Ferroelectric-Graphene Heterostructures*, Doctoral dissertation, The University of Nebraska – Lincoln, 2024.

140 M. Hoffmann, M. Pešić, S. Slesazeck, U. Schroeder and T. Mikolajick, On the stabilization of ferroelectric negative capacitance in nanoscale devices, *Nanoscale*, 2018, **10**, 10891–10899.

141 S. Salahuddin and S. Datta, Use of Negative Capacitance to Provide Voltage Amplification for Low Power Nanoscale Devices, *Nano Lett.*, 2008, **8**, 405–410.

142 K. Majumdar, S. Datta and S. P. Rao, Revisiting the Theory of Ferroelectric Negative Capacitance, *IEEE Trans. Electron Devices*, 2016, **63**, 2043–2049.

143 A. I. Khan, K. Chatterjee, B. Wang, S. Drapcho, L. You, C. Serrao, S. R. Bakaul, R. Ramesh and S. Salahuddin, Negative capacitance in a ferroelectric capacitor, *Nat. Mater.*, 2015, **14**, 182–186.

144 S.-C. Chang, U. E. Avci, D. E. Nikonov, S. Manipatruni and I. A. Young, Physical Origin of Transient Negative Capacitance in a Ferroelectric Capacitor, *Phys. Rev. Appl.*, 2018, **9**, 014010.

145 M. Hoffmann, F. P. G. Fengler, M. Herzig, T. Mittmann, B. Max, U. Schroeder and R. Negrea, P. Lucian, S. Slesazeck and T. Mikolajick, Unveiling the double-well energy landscape in a ferroelectric layer, *Nature*, 2019, **565**, 464–467.

146 J. Íñiguez, P. Zubko, I. Luk'yanchuk and A. Cano, Ferroelectric negative capacitance, *Nat. Rev. Mater.*, 2019, **4**, 243–256.

147 J. Y. Jo, H. S. Han, J. G. Yoon, T. K. Song, S. H. Kim and T. W. Noh, Domain Switching Kinetics in Disordered Ferroelectric Thin Films, *Phys. Rev. Lett.*, 2007, **99**, 267602.

148 H. Lu, B. Wang, T. Li, A. Lipatov, H. Lee, A. Rajapitamahuni, R. Xu, X. Hong, S. Farokhipoor, L. W. Martin, C.-B. Eom, L.-Q. Chen, A. Sinitskii and A. Gruverman, Nanodomain Engineering in Ferroelectric Capacitors with Graphene Electrodes, *Nano Lett.*, 2016, **16**, 6460–6466.

149 H. Chen, T. Li, Y. Hao, A. Rajapitamahuni, Z. Xiao, S. Schoeche, M. Schubert and X. Hong, Remote surface optical phonon scattering in ferroelectric $Ba_{0.6}Sr_{0.4}TiO_3$ gated graphene, *J. Appl. Phys.*, 2022, **132**, 154301.

150 M. V. Fischetti, D. A. Neumayer and E. A. Cartier, Effective electron mobility in Si inversion layers in metal-oxide-semiconductor systems with a high-κ insulator:: The role of remote phonon scattering, *J. Appl. Phys.*, 2001, **90**, 4587–4608.

151 K. Zou, X. Hong, D. Keefer and J. Zhu, Deposition of High-Quality HfO_2 on Graphene and the Effect of Remote Oxide Phonon Scattering, *Phys. Rev. Lett.*, 2010, **105**, 126601.

152 M. Barbier, P. Vasilopoulos and F. M. Peeters, Single-layer and bilayer graphene superlattices: collimation, additional Dirac points and Dirac lines, *Philos. Trans. R. Soc., A*, 2010, **368**, 5499–5524.

153 A. N. Rudenko and M. I. Katsnelson, Anisotropic effects in two-dimensional materials, *2D Mater.*, 2024, **11**, 042002.

154 C.-H. Park, Y.-W. Son, L. Yang, M. L. Cohen and S. G. Louie, Electron Beam Supercollimation in Graphene Superlattices, *Nano Lett.*, 2008, **8**, 2920–2924.

155 C.-H. Park, L. Yang, Y.-W. Son, M. L. Cohen and S. G. Louie, Anisotropic behaviours of massless Dirac fermions in graphene under periodic potentials, *Nat. Phys.*, 2008, **4**, 213–217.

156 S. Dubey, V. Singh, A. K. Bhat, P. Parikh, S. Grover, R. Sensarma, V. Tripathi, K. Sengupta and M. M. Deshmukh, Tunable Super-lattice in Graphene To Control the Number of Dirac Points, *Nano Lett.*, 2013, **13**, 3990–3995.

157 Y. Li, S. Dietrich, C. Forsythe, T. Taniguchi, K. Watanabe, P. Moon and C. R. Dean, Anisotropic band flattening in graphene with one-dimensional superlattices, *Nat. Nanotechnol.*, 2021, **16**, 525–530.

158 H. S. Lee, S. W. Min, M. K. Park, Y. T. Lee, P. J. Jeon, J. H. Kim, S. Ryu and S. Im, MoS_2 Nanosheets for Top-Gate Nonvolatile Memory Transistor Channel, *Small*, 2012, **8**, 3111–3115.

159 C. J. Zhou, X. S. Wang, S. Raju, Z. Y. Lin, D. Villaroman, B. L. Huang, H. L. W. Chan, M. S. Chan and Y. Chai, Low voltage and high ON/OFF ratio field-effect transistors based on CVD MoS_2 and ultra high-k gate dielectric PZT, *Nanoscale*, 2015, **7**, 8695–8700.

160 F. A. McGuire, Z. H. Cheng, K. Price and A. D. Franklin, Sub-60 mV/decade switching in 2D negative capacitance field-effect transistors with integrated ferroelectric polymer, *Appl. Phys. Lett.*, 2016, **109**, 093101.

161 Z. Y. Lu, C. Serrao, A. I. Khan, L. You, J. C. Wong, Y. Ye, H. Y. Zhu, X. Zhang and S. Salahuddinl, Nonvolatile MoS_2 field effect transistors directly gated by single crystalline epitaxial ferroelectric, *Appl. Phys. Lett.*, 2017, **111**, 023104.

162 X. Wang, Y. Chen, G. Wu, D. Li, L. Tu, S. Sun, H. Shen, T. Lin, Y. Xiao, M. Tang, W. Hu, L. Liao, P. Zhou, J. Sun, X. Meng, J. Chu and J. Wang, Two-dimensional negative capacitance transistor with polyvinylidene fluoride-based ferroelectric polymer gating, *npj 2D Mater. Appl.*, 2017, **1**, 38.

163 F. A. McGuire, Y. C. Lin, K. Price, G. B. Rayner, S. Khandelwal, S. Salahuddin and A. D. Franklin, Sustained Sub-60 mV decade^{-1} Switching *via* the Negative Capacitance Effect in MoS_2 Transistors, *Nano Lett.*, 2017, **17**, 4801–4806.

164 A. Nourbakhsh, A. Zubair, S. Joglekar, M. Dresselhaus and T. Palacios, Subthreshold swing improvement in MoS_2 transistors by the negative-capacitance effect in a ferroelectric Al-doped-HfO_2/HfO_2 gate dielectric stack, *Nanoscale*, 2017, **9**, 6122–6127.

165 M. Si, C. Jiang, C. Su, Y. Tang, L. Yang, W. Chung, M. A. Alam and P. D. Ye, Sub-60 mV dec^{-1} ferroelectric HZO MoS_2 negative capacitance field-effect transistor with internal metal gate: The role of parasitic capacitance. In Proc. 2017 IEEE International Electron Devices Meeting (IEDM) 23.5.1–23.5.4 (IEEE, 2017).

166 Z. Yu, H. Wang, W. Li, S. Xu, X. Song, S. Wang, P. Wang, P. Zhou, Y. Shi, Y. Chai and X. Wang, Negative capacitance 2D MoS_2 transistors with sub-60 mV dec^{-1} subthreshold swing over 6 orders, 250 µA µm^{-1} current density, and nearly-hysteresis-free. In Proc. 2017 IEEE International Electron Devices Meeting (IEDM) 23.6.1–23.6.4 (IEEE, 2017).

167 X. Q. Liu, R. R. Liang, G. Y. Gao, C. F. Pan, C. S. Jiang, Q. Xu, J. Luo, X. M. Zou, Z. Y. Yang, L. Liao and Z. L. Wang, MoS_2 Negative-Capacitance Field-Effect Transistors with Subthreshold Swing below the Physics Limit, *Adv. Mater.*, 2018, **30**, 1800932.

168 M. W. Si, C. J. Su, C. S. Jiang, N. J. Conrad, H. Zhou, K. D. Maize, G. Qiu, C. T. Wu, A. Shakouri, M. A. Alam and P. D. Ye, Steep-slope hysteresis-free negative capacitance MoS_2 transistors, *Nat. Nanotechnol.*, 2018, **13**, 24.

169 B. Meyer and D. Vanderbilt, *Ab initio* study of ferroelectric domain walls in $PbTiO_3$, *Phys. Rev. B: Condens. Matter Mater. Phys.*, 2002, **65**, 104111.

170 C. L. Jia, K. W. Urban, M. Alexe, D. Hesse and I. Vrejoiu, Direct Observation of Continuous Electric Dipole Rotation in Flux-Closure Domains in Ferroelectric $Pb(Zr,Ti)O_3$, *Science*, 2011, **331**, 1420–1423.

171 S. Choudhury, Y. L. Li, C. E. Krill and L. Q. Chen, Phase-field simulation of polarization switching and domain evolution in ferroelectric polycrystals, *Acta Mater.*, 2005, **53**, 5313–5321.

172 C. H. Li, K. M. McCreary and B. T. Jonker, Spatial Control of Photoluminescence at Room Temperature by Ferroelectric Domains in Monolayer WS_2/PZT Hybrid Structures, *ACS Omega*, 2016, **1**, 1075–1080.

173 B. Wen, Y. Zhu, D. Yudistira, A. Boes, L. Zhang, T. Yidirim, B. Liu, H. Yan, X. Sun, Y. Zhou, Y. Xue, Y. Zhang, L. Fu, A. Mitchell, H. Zhang and Y. Lu, Ferroelectric-Driven Exciton and Trion Modulation in Monolayer Molybdenum and Tungsten Diselenides, *ACS Nano*, 2019, **13**, 5335–5343.

174 S. Cherifi-Hertel, H. Bulou, R. Hertel, G. Taupier, K. D. H. Dorkenoo, C. Andreas, J. Guyonnet, I. Gaponenko, K. Gallo and P. Paruch, Non-Ising and chiral ferroelectric domain walls revealed by nonlinear optical microscopy, *Nat. Commun.*, 2017, **8**, 15768.

175 G. De Luca, M. D. Rossell, J. Schaab, N. Viart, M. Fiebig and M. Trassin, Domain Wall Architecture in Tetragonal Ferroelectric Thin Films, *Adv. Mater.*, 2017, **29**, 1605145.

176 Y. Li, Y. Rao, K. F. Mak, Y. You, S. Wang, C. R. Dean and T. F. Heinz, Probing Symmetry Properties of Few-Layer MoS_2 and h-BN by Optical Second-Harmonic Generation, *Nano Lett.*, 2013, **13**, 3329–3333.

177 I. Studenyak, V. Mitrovcij, G. S. Kovacs, M. Gurzan, O. Mykajlo, Y. M. Vysochanskii and V. Cajipe, Disordering effect on optical absorption processes in $CuInP_2S_6$ layered ferrielectrics, *Phys. Status Solidi B*, 2003, **236**, 678–686.

178 L. You, Y. Zhang, S. Zhou, A. Chaturvedi, S. A. Morris, F. Liu, L. Chang, D. Ichinose, W. Funakubo, W. Hu, T. Wu, Z. Liu, S. Dong and J. Wang, Origin of giant negative piezoelectricity in a layered van der Waals ferroelectric, *Sci. Adv.*, 2019, **5**, eaav3780.

179 S. Zhou, L. You, H. Zhou, Y. Pu, Z. Gui and J. Wang, van der Waals layered ferroelectric $CuInP_2S_6$: physical properties and device applications, *Front. Phys.*, 2021, **16**, 1–30.

180 J. A. Brehm, S. M. Neumayer, L. Tao, A. O'Hara, M. Chyasnavichus, M. A. Susner, M. A. McGuire, S. V. Kalinin, S. Jesse, P. Ganesh, S. T. Pantelides, P. Maksymovych and N. Balke, Tunable quadruple-well ferroelectric van der Waals crystals, *Nat. Mater.*, 2020, **19**, 43–48.

181 D.-D. Xu, R.-R. Ma, Y.-F. Zhao, Z. Guan, Q.-L. Zhong, R. Huang, P.-H. Xiang, N. Zhong and C.-G. Duan, Unconventional out-of-plane domain inversion *via* in-plane ionic migration in a van der Waals ferroelectric, *J. Mater. Chem. C*, 2020, **8**, 6966–6971.

182 D. Zhang, Z.-D. Luo, Y. Yao, P. Schoenherr, C. Sha, Y. Pan, P. Sharma, M. Alexe and J. Seidel, Anisotropic ion migration and electronic conduction in van der Waals ferroelectric $CuInP_2S_6$, *Nano Lett.*, 2021, **21**, 995–1002.

183 X. Hou, F. Kong, Y. Tong, H. Li, J. Dai, Y. Li, H. Huang, C. Sun, J. Gao, L. Pan and D. Li, Optical Evidence of Interfacial Strain-Induced Ferroelectric Tuning and Enhancement in $CuInP_2S_6$ *via* Ferroelectric Substrate, *Small*, 2025, 2409879.

184 H. Zhu, K. Miyata, Y. Fu, J. Wang, P. P. Joshi, D. Niesner, K. W. Williams, S. Jin and X.-Y. Zhu, Screening in crystalline liquids protects energetic carriers in hybrid perovskites, *Science*, 2016, **353**, 1409–1413.

185 H. Yoon, T. K. Truttmann, F. Liu, B. E. Matthews, S. Choo, Q. Su, V. Saraswat, S. Manzo, M. S. Arnold, M. E. Bowden, J. K. Kawasaki, S. J. Koester, S. R. Spurgeon, S. A. Chambers and B. Jalan, Free-standing epitaxial $SrTiO_3$ nanomembranes *via* remote epitaxy using hybrid molecular beam epitaxy, *Sci. Adv.*, 2022, **8**, eadd5328.

186 C. S. Chang, K. S. Kim, B.-I. Park, J. Choi, H. Kim, J. Jeong, M. Barone, N. Parker, S. Lee, X. Zhang, K. Lu, J. M. Suh, J. Kim, D. Lee, N. M. Han, M. Moon, Y. S. Lee, D.-H. Kim, D. G. Schlom, Y. J. Hong and J. Kim, Remote epitaxial interaction through graphene, *Sci. Adv.*, 2023, **9**, eadj5379.

187 Y. Li, C. Xiang, F. M. Chiabrera, S. Yun, H. Zhang, D. J. Kelly, R. T. Dahm, C. K. R. Kirchert, T. E. L. Cozannet, F. Trier, D. V. Christensen, T. J. Booth, S. B. Simonsen, S. Kadkhodazadeh, T. S. Jespersen and N. Pryds, Stacking and Twisting of Freestanding Complex Oxide Thin Films, *Adv. Mater.*, 2022, **34**, 2203187.

188 F. He, Y. Zhou, Z. Ye, S. H. Cho, J. Jeong, X. Meng and Y. Wang, Moiré Patterns in 2D Materials: A Review, *ACS Nano*, 2021, **15**, 5944–5958.

189 N. A. Shahed, K. Samanta, M. Elekhtiar, K. Huang, C.-B. Eom, M. S. Rzchowski, K. D. Belashchenko and E. Y. Tsymbal, Prediction of polarization vortices, charge modulation, flat bands, and moiré magnetism in twisted oxide bilayers, *arXiv*, 2024, arXiv:2412.03798.

190 J. P. B. Silva, R. Alcala, U. E. Avci, N. Barrett, L. Bégon-Lours, M. Borg, S. Byun, S.-C. Chang, S.-W. Cheong, D.-H. Choe, J. Coignus, V. Deshpande, A. Dimoulas, C. Dubourdieu, I. Fina, H. Funakubo, L. Grenouillet, A. Gruverman, J. Heo, M. Hoffmann, H. A. Hsain, F.-T. Huang, C. S. Hwang, J. Íñiguez, J. L. Jones, I. V. Karpov, A. Kersch, T. Kwon, S. Lancaster, M. Lederer, Y. Lee, P. D. Lomenzo, L. W. Martin, S. Martin, S. Migita, T. Mikolajick, B. Noheda, M. H. Park, K. M. Rabe, S. Salahuddin, F. Sánchez, K. Seidel, T. Shimizu, T. Shiraishi, S. Slesazeck, A. Toriumi, H. Uchida, B. Vilquin, X. Xu, K. H. Ye and U. Schroeder, Roadmap on ferroelectric hafnia- and zirconia-based materials and devices, *APL Mater.*, 2023, **11**, 089201.

191 Y. Yun, P. Buragohain, M. Li, Z. Ahmadi, Y. Zhang, X. Li, H. Wang, J. Li, P. Lu, L. Tao, H. Wang, J. E. Shield, E. Y. Tsymbal, A. Gruverman and X. Xu, Intrinsic ferroelectricity in Y-doped HfO_2 thin films, *Nat. Mater.*, 2022, **21**, 903–909.

192 X. Hong, Ferroelectric hafnia surface in action, *Nat. Mater.*, 2023, **22**, 1049–1050.

193 K. P. Kelley, A. N. Morozovska, E. A. Eliseev, Y. Liu, S. S. Fields, S. T. Jaszewski, T. Mimura, S. Calderon, E. C. Dickey, J. F. Ihlefeld and S. V. Kalinin, Ferroelectricity in hafnia controlled *via* surface electrochemical state, *Nat. Mater.*, 2023, **22**, 1144–1151.

194 H.-J. Lee, M. Lee, K. Lee, J. Jo, H. Yang, Y. Kim, S. C. Chae, U. Waghmare and J. H. Lee, Scale-free ferroelectricity induced by flat phonon bands in HfO_2, *Science*, 2020, **369**, 1343–1347.

195 S. Zhou, J. Zhang and A. M. Rappe, Strain-induced antipolar phase in hafnia stabilizes robust thin-film ferroelectricity, *Sci. Adv.*, 2022, **8**, eadd5953.

196 L. L. Tao and E. Y. Tsymbal, Persistent spin texture enforced by symmetry, *Nat. Commun.*, 2018, **9**, 2763.

197 G. Viswan, K. Wang, R. Streubel, X. Hong, N. Valanoor, D. Sando and P. A. Dowben, Magnetocapacitance at the Ni/$BiInO_3$ Schottky Interface, *ACS Appl. Mater. Interfaces*, 2024, **16**, 4108–4116.

198 M. Acharya, S. Mack, A. Fernandez, J. Kim, H. Y. Wang, K. Eriguchi, D. Meyers, V. Gopalan, J. Neaton and L. W. Martin, Searching for New Ferroelectric Materials Using High-Throughput Databases: An Experimental Perspective on $BiAlO_3$ and $BiInO_3$, *Chem. Mater.*, 2020, **32**, 7274–7283.

199 N. A. Benedek and C. J. Fennie, Why Are There So Few Perovskite Ferroelectrics?, *J. Phys. Chem. C*, 2013, **117**, 13339–13349.

200 J. M. Rondinelli, S. J. May and J. W. Freeland, Control of octahedral connectivity in perovskite oxide heterostructures: An emerging route to multifunctional materials discovery, *MRS Bull.*, 2012, **37**, 261–270.

201 H. Wang, J. Wen, D. J. Miller, Q. Zhou, M. Chen, H. N. Lee, K. M. Rabe and X. Wu, Stabilization of Highly Polar $BiFeO_3$-like Structure: A New Interface Design Route for Enhanced Ferroelectricity in Artificial Perovskite Superlattices, *Phys. Rev. X*, 2016, **6**, 011027.